A comparison of two causal methods in the context of climate analyses

David Docquier[1], Giorgia Di Capua[2,3], Reik V. Donner[2,3], Carlos A. L. Pires[4], Amélie Simon[4], and Stéphane Vannitsem[1]

[1]Royal Meteorological Institute of Belgium, Brussels, Belgium
[2]Potsdam Institute for Climate Impact Research, Potsdam, Germany
[3]Magdeburg-Stendal University of Applied Sciences, Magdeburg, Germany
[4]Instituto Dom Luiz, Faculdade de Ciências, Universidade de Lisboa, Lisbon, Portugal

Correspondence: D. Docquier (david.docquier@meteo.be)

Abstract. Correlation does not necessarily imply causation, and this is why causal methods have been developed to try to disentangle true causal links from spurious relationships. In our study, we use two causal methods, namely the Liang-Kleeman information flow (LKIF) and the Peter and Clark momentary conditional independence (PCMCI) algorithm, and apply them to four different artificial models of increasing complexity and one real-case study based on climate indices in the North Atlantic and North Pacific. We show that both methods are superior to the classical correlation analysis, especially in removing spurious links. LKIF and PCMCI display some strengths and weaknesses for the three simplest models, with LKIF performing better with a smaller number of variables, and PCMCI being best with a larger number of variables. Detecting causal links from the fourth model is more challenging as the system is nonlinear and chaotic. For the real-case study with climate indices, both methods present some similarities and differences at monthly time scale. One of the key differences is that LKIF identifies the Arctic Oscillation (AO) as the largest driver, while El Niño-Southern Oscillation (ENSO) is the main influencing variable for PCMCI. More research is needed to confirm these links, in particular including nonlinear causal methods.

1 Introduction

One of the most commonly used methodologies to identify potential relationships between variables in climate research is the correlation, with or without a lag (or time delay). For example, Bishop et al. (2017) used an approach based on lead-lag correlations between sea-surface temperature (SST) and turbulent heat flux to discriminate between atmospheric-driven and ocean-led variability using both a stochastic energy balance model and satellite observations at monthly time scale. In another study, Docquier et al. (2019) found a systematic large anti-correlation between Arctic sea-ice area and northward ocean heat transport in climate models at different resolutions, which confirmed previous observational findings showing that the latter is a driver of the former (Årthun et al., 2012). Another example is the modeling analysis from Small et al. (2020), who used a regression analysis to quantify the dynamical and thermodynamical contributions to the ocean heat content tendency at the global scale.

However, such correlation (or regression) approaches, despite being useful for identifying potential relationships between variables, do not imply causation. A significant correlation simply means that there is a relationship, or synchronous behavior, between two variables without explicitly confirming a causal link between the two. Correlation suffers from five key limitations. First, a significant correlation between variables could appear by chance (that is called 'random coincidence'). Second, the correlation does not allow to identify the direction of the potential causal link, so this approach supposes an a priori knowledge of processes at play. Third, there could be an external (hidden) variable (sometimes referred to as a 'confounding variable') that influences two correlated variables, as demonstrated in Sugihara et al. (2012), and a simple correlation analysis would not allow for disentangling these causal links. Fourth, the correlation cannot identify possible nonlinear relationships. Lastly, the correlation is computed for pairs of variables and does not consider multivariate frameworks.

Hence, causal methods prove to be very useful. Runge et al. (2019a) provide a detailed review of causal inference frameworks applied to Earth system sciences, despite excluding one of the causal methods used here. Some of these methods are briefly described hereafter. Granger causality is the first formalization of causality to time series and is based on autoregressive modeling (Granger, 1969). It has been used in a series of climate studies, including several analyses focusing on air-sea interactions (Mosedale et al., 2006; Tirabassi et al., 2015; Bach et al., 2019). Convergent-cross mapping (CCM) attempts to uncover causal relationships based on Taken's theorem and nonlinear state-space reconstruction (Sugihara et al., 2012). For example, CCM has been used for analyzing the temperature-CO_2 relationship over glacial-interglacial timescales (van Nes et al., 2015), the causal dependencies between different ocean basins (Vannitsem and Ekelmans, 2018), and the stratosphere-troposphere coupling (Huang et al., 2020). Transfer entropy (Schreiber, 2000) and conditional mutual information (CMI; Paluš et al. 2001; Paluš and Vejmelka 2007) are also two widely used causal methods, which have been proved to be equivalent (Paluš and Vejmelka, 2007). Silini et al. (2022) have used a fast alternative of transfer entropy, called pseudo-transfer entropy, to quantify causal dependencies between 13 climate indices representing large-scale climate patterns.

The PCMCI method is a causal discovery method based on the Peter and Clark (PC) algorithm (Spirtes et al., 2001), combined with the momentary conditional independence (MCI) approach (Runge et al., 2019b). PCMCI has been used, for example, to analyze Arctic drivers of mid-latitude winter circulation (Kretschmer et al., 2016), relationships between Niño3.4 and extratropical air temperature over British Columbia (Runge et al., 2019b), tropical and mid-latitude drivers of the Indian summer monsoon (Di Capua et al., 2020a), predictors for seasonal Atlantic hurricane activity (Pfleiderer et al., 2020), and interactions between tropical convection and mid-latitude circulation (Di Capua et al., 2020b).

The Liang-Kleeman information flow (LKIF; Liang and Kleeman 2005) is based on the rate of information transfer in dynamical systems and has been rigorously derived from the propagation of information entropy between variables (Liang, 2016). This method has been applied to several climate studies, including the El Niño - Indian Ocean Dipole (IOD) link (Liang, 2014), the relationship between carbon dioxide and air temperature (Jiang et al., 2019; Hagan et al., 2022), dynamical dependencies between a set of observables and the Antarctic surface mass balance (Vannitsem et al., 2019), identification of potential drivers of Arctic sea-ice changes (Docquier et al., 2022), causal links between climate indices in the North Pacific and Atlantic regions and local Belgian time series (Vannitsem and Liang, 2022), and ocean-atmosphere interactions (Docquier et al., 2023).

Generally, each study focuses on only one causal method. However, contradictory results might appear when using different causal methods, and it is thus important to compare them. Several studies have investigated differences between causal methods. One of the most comprehensive studies in this respect in the recent past is the intercomparison of Krakovská et al. (2018), in
60   which the authors compared six causal methods, namely Granger causality, two extended versions of Granger causality, CMI, CCM, and predictability improvement (Krakovská and Hanzely, 2016). They used seven artificial datasets based on coupled systems. A key outcome of their analysis is that there is no single best causal method as results depend on the intrinsic characteristics of the used dataset. Krakovská et al. (2018) found that for simple autoregressive models, Granger causality and its extensions were the best tools to identify the right causal links, while CCM and predictability improvement failed. On
65   the contrary, for more complex systems, Granger causality and its extensions failed, while the remaining methods were more successful, although they differed considerably in their ability to detect the presence and direction of coupling. Paluš et al. (2018) showed that the Granger causality principle that the cause precedes the effect was violated in coupled chaotic dynamical systems using CMI, CCM and predictability improvement. Coufal et al. (2017) used CMI and CCM, and showed that the detection of coupling delays in coupled nonlinear dynamical systems was challenging. Manshour et al. (2021) compared CMI
70   with LKIF and interventional causality (Baldovin et al., 2020), and confirmed a robust influence of solar wind on geomagnetic indices using all causal methods. An advantage of interventional causality compared to other causal methods is the detection of indirect causal links (i.e., if x influences y and y drives z, the indirect influence from x to z will be recovered).

The main goal of this study is to provide a detailed comparison between two independent causal methods, namely LKIF and PCMCI, which have been widely used in the context of the JPI-Climate/JPI-Oceans ROADMAP project (Role of ocean
75   dynamics and Ocean-Atmosphere interactions in Driving cliMAte variations and future Projections of impact-relevant extreme events; https://jpi-climate.eu/project/roadmap/) and have never been methodically compared together before. In this analysis, we use these two methods in the same framework to allow a fair comparison. We also compute the correlation coefficient to show the superiority of causal methods compared to a classical correlation analysis. In particular, we use four different artificial models with an increasing level of complexity and one real-case study based on climate indices. These different datasets are
80   described in Sect. 2, and our two causal methods are presented in Sect. 3. Results of our comparison are presented in Sect. 4 and a discussion is provided in Sect. 5, before concluding in Sect. 6.

2   Data

In order to apply the two causal methods described below (Sect. 3), we use three different stochastic models (including two linear models and one nonlinear model), one deterministic nonlinear model (Lorenz, 1963), and one real-case study using
85   climate indices in the North Atlantic and North Pacific. This allows us to test LKIF and PCMCI with an increasing level of complexity (from a simple two-dimensional model to a real-case study).

2.1 Two-dimensional (2D) model

We first consider a two-dimensional (2D) stochastic linear model (Eq. (12) in Liang 2014):

$$
\begin{aligned}
\mathrm{d}x_1 &= (-x_1 + 0.5\,x_2)\,\mathrm{d}t + 0.1\,\mathrm{d}w_1, \\
\mathrm{d}x_2 &= -x_2\,\mathrm{d}t + 0.1\,\mathrm{d}w_2,
\end{aligned}
\tag{1}
$$

where x_1 and x_2 are the two variables, t is time, and w_1 and w_2 represent standard Wiener processes in x_1 and x_2, respectively ($\mathrm{d}w_k \sim \sqrt{\mathrm{d}t}\,N(0,1)$, with $N(0,1)$ being a normal distribution with zero mean and unit variance). In this simple system, x_2 drives x_1, but not vice versa (Fig. 1(f)).

We solve this system with the Euler-Maruyama method using a time step $\mathrm{d}t = 0.001$ and 1000 unit times, which brings 10^6 time steps. We initialize the system with $x_1(0) = 1$ and $x_2(0) = 2$. For our analysis, we discard the first 10 unit times (first 10^4 time steps), which is considered to be our spin-up period.

2.2 Six-dimensional (6D) model

Then, we investigate a six-dimensional (6D) stochastic linear vector autoregressive (VAR) model with only one lag (Eq. (21) in Liang 2021):

$$
\begin{aligned}
x_{1,t+1} &= 0.1 - 0.6\,x_{3,t} + u_{1,t+1}, \\
x_{2,t+1} &= 0.7 - 0.5\,x_{1,t} + 0.8\,x_{6,t} + u_{2,t+1}, \\
x_{3,t+1} &= 0.5 + 0.7\,x_{2,t} + u_{3,t+1}, \\
x_{4,t+1} &= 0.2 + 0.7\,x_{4,t} + 0.4\,x_{5,t} + u_{4,t+1}, \\
x_{5,t+1} &= 0.8 + 0.2\,x_{4,t} + 0.7\,x_{6,t} + u_{5,t+1}, \\
x_{6,t+1} &= 0.3 - 0.5\,x_{6,t} + u_{6,t+1},
\end{aligned}
\tag{2}
$$

where x_k ($k = 1, ..., 6$) are the six variables, and u_k are normal random noises in these six variables ($u_k \sim N(0,1)$). By construction, we have two directed cycles, i.e. $x_1 \rightarrow x_2 \rightarrow x_3 \rightarrow x_1$ and $x_4 \rightarrow x_5 \rightarrow x_4$, and these cycles are driven by a common cause, i.e. x_6, which drives both x_2 and x_5 (Fig. 2(d)).

We solve this system using 10^6 time steps ($\mathrm{d}t = 1$). For our analysis, we discard the first 10^4 time steps.

2.3 Nine-dimensional (9D) model

The next model is a nine-dimensional (9D) stochastic nonlinear VAR system with a maximum of four lags (Eq. (17) in Subramaniyam et al. 2021):

$$
\begin{aligned}
x_{1,t} &= 3.4\,x_{1,t-1}\,(1-x_{1,t-1}^2)\,e^{-x_{1,t-1}^2}+2.5\,x_{2,t-4}+1.8\,x_{3,t-2}+1.5\,x_{4,t-2}+0.4\,u_{1,t}, \\
x_{2,t} &= 3.4\,x_{2,t-1}\,(1-x_{2,t-1}^2)\,e^{-x_{2,t-1}^2}+0.4\,u_{2,t}, \\
x_{3,t} &= 3.4\,x_{3,t-1}\,(1-x_{3,t-1}^2)\,e^{-x_{3,t-1}^2}+0.25\,x_{1,t-1}+0.4\,u_{3,t}, \\
x_{4,t} &= 3.4\,x_{4,t-1}\,(1-x_{4,t-1}^2)\,e^{-x_{4,t-1}^2}+1.5\,x_{5,t-3}+1.2\,x_{6,t-1}+0.4\,u_{4,t}, \\
x_{5,t} &= 3.4\,x_{5,t-1}\,(1-x_{5,t-1}^2)\,e^{-x_{5,t-1}^2}+0.4\,u_{5,t}, \\
x_{6,t} &= 3.4\,x_{6,t-1}\,(1-x_{6,t-1}^2)\,e^{-x_{6,t-1}^2}+1.5\,x_{7,t-3}+0.4\,u_{6,t}, \\
x_{7,t} &= 3.4\,x_{7,t-1}\,(1-x_{7,t-1}^2)\,e^{-x_{7,t-1}^2}+0.4\,u_{7,t}, \\
x_{8,t} &= 3.4\,x_{8,t-1}\,(1-x_{8,t-1}^2)\,e^{-x_{8,t-1}^2}+0.8\,x_{7,t-1}+0.4\,u_{8,t}, \\
x_{9,t} &= 3.4\,x_{9,t-1}\,(1-x_{9,t-1}^2)\,e^{-x_{9,t-1}^2}+1.8\,x_{7,t-1}+0.4\,u_{9,t},
\end{aligned}
\tag{3}
$$

where x_k $(k=1,...,9)$ are the nine variables, e is the exponential function and u_k are normal random noises in these nine variables ($u_k \sim N(0,1)$). This system contains a directed chain $x_7 \rightarrow x_6 \rightarrow x_4 \rightarrow x_1 \rightarrow x_3$ and a fork, i.e. x_7 driving x_6, x_8 and x_9. There are also two colliders, with x_5 and x_6 both affecting x_4 on the one hand, and x_2, x_3 and x_4 driving x_1 on the other hand (Fig. 4(d)). A particularity of this system compared to the 6D model (Eq. (2)) is the presence of lags larger than one.

We solve this system using 10^6 time steps (dt = 1). For our analysis, we discard the first 10^4 time steps.

2.4 Lorenz (1963) model

We also use the three-dimensional (3D) Lorenz (1963) model, which is deterministic, nonlinear and non-periodic, and is a simplified model representing atmospheric convection:

$$
\begin{aligned}
\frac{\mathrm{d}x}{\mathrm{d}t} &= 10\,(y-x), \\
\frac{\mathrm{d}y}{\mathrm{d}t} &= 28\,x - y - x\,z, \\
\frac{\mathrm{d}z}{\mathrm{d}t} &= x\,y - \frac{8}{3}\,z,
\end{aligned}
\tag{4}
$$

where x, y and z are the three variables and are proportional to the convection intensity, the horizontal temperature variation and the vertical temperature variation, respectively. We use the standard parameters of the model.

We solve the Lorenz (1963) model using the fourth-order Runge-Kutta scheme, a time step dt = 0.01 and 1000 unit times, which brings 10^5 time steps. We initialize the system with $x(0) = 0$, $y(0) = 1$ and $z(0) = 0$. For our analysis, we discard the first 100 unit times (first 10^4 time steps; spin-up period).

2.5 Climate indices

140 Finally, we use eight different global climate indices spanning the North Atlantic and North Pacific regions, following a similar approach as Vannitsem and Liang (2022) and Silini et al. (2022). Four of these indices are atmospheric and four of them are oceanic. Time series of these indices were retrieved from the Physical Sciences Laboratory (PSL) of the National Oceanic and Atmospheric Administration (NOAA; https://psl.noaa.gov/data/climateindices/list/). We use monthly values from January 1950 to December 2021 (864 months), and we remove the linear trend in order to get relatively stationary time series, which is 145 a requirement for applying our causal methods.

The four atmospheric indices are computed from the National Centers for Environmental Prediction / National Center for Atmospheric Research (NCEP/NCAR) reanalysis:

– The Pacific North American (PNA) index is obtained by projecting the daily 500 hPa geopotential height anomalies over the Northern Hemisphere (0-90°N) onto the PNA loading pattern (second leading mode of rotated Empirical Orthogonal 150 Function [EOF] analysis of monthly mean 500 hPa height anomalies during the 1950-2000 period). A positive PNA features above-average heights in the vicinity of Hawaii and over the intermountain region of North America, and below-average heights south of the Aleutian Islands and over the southeastern United States. A negative PNA reflects an opposite pattern of height anomalies over these regions.

– The North Atlantic Oscillation (NAO) is based on the difference in sea-level pressure between the Subtropical High 155 (Azores) and the Subpolar Low (Iceland). A positive NAO reflects above-normal pressure over the central North Atlantic, the eastern United States and western Europe, and below-normal pressure across high latitudes of the North Atlantic. A negative NAO features an opposite pattern of pressure anomalies over these regions.

– The Arctic Oscillation (AO), or Northern Annular Mode (NAM), is constructed by projecting the 1000 hPa geopotential height anomalies poleward of 20°N onto the leading EOF (using monthly mean 1000 hPa height anomalies from 1979 160 to 2000). When the AO is in its positive phase, strong westerlies act to confine colder air across polar regions. When the AO is negative, the westerly jet weakens and can become more meandering.

– The Quasi-Biennal Oscillation (QBO) is calculated from the zonal average of the 30 hPa zonal wind at the equator. It is the most predictable mode of atmospheric variability that is not linked to changing seasons, with easterly and westerly winds alternating each 13 months.

165 Below are the four oceanic indices:

– The Atlantic Multidecadal Oscillation (AMO) is computed based on version 2 of the Kaplan et al. (1998) extended SST gridded dataset (which uses UK Met Office SST data) averaged over the North Atlantic (0-70°N; unsmoothed time series) and following the procedure described in Enfield et al. (2001). Cool and warm phases of the AMO may alternate every 20-40 years.

170   – The Pacific Decadal Oscillation (PDO) is obtained by projecting the Pacific SST anomalies from version 5 of the NOAA Extended Reconstructed SST (ERSST) dataset onto the dominant EOF from 20°N to 60°N. The PDO is positive when SST is anomalously cold in the interior North Pacific and warm along the Pacific Coast. The PDO is negative when the climate anomaly patterns are reversed.

    – The Tropical North Atlantic (TNA) index is computed based on SST anomalies from the Hadley Centre Global Sea Ice
175   and Sea Surface Temperature (HadISST) and NOAA Optimal Interpolation (OI) datasets averaged in the Tropical North Atlantic (5.5-23.5°N; 57.5-15°W), based on Enfield et al. (1999).

    – The Niño3.4 index is based on standardized SST anomalies (using ERSST v5) averaged over the eastern tropical Pacific (5°S-5°N; 170-120°W). The Niño3.4 index is in its warm phase when SST anomaly exceeds 0.5°C, and it is in its cold phase when SST anomaly is below -0.5°C. For the remainder of the paper, we will refer to this index as 'ENSO' (El
180   Niño-Southern Oscillation), as it is closely associated with this oscillation.

3   Methods

In this section, we describe the two causal methods used in this study, namely the Liang-Kleeman information flow (LKIF) and the Peter and Clark momentary conditional independence (PCMCI) methods. We compare our results to the more traditional Pearson correlation coefficient, which is the covariance between two variables divided by the product of their standard
185   deviations.

3.1   Liang-Kleeman information flow (LKIF)

The LKIF method has been developed by Liang and Kleeman (2005). It has been first applied in bivariate cases (Liang and Kleeman, 2005; Liang, 2014) and has subsequently been extended to multivariate cases (Liang, 2016, 2021). In our study, we use the multivariate formulation of LKIF. In this framework, causal inference is based on information flow, which has been
190   recognized as a real physical notion, i.e. formulated from first principles of information theory (Liang, 2016).

Under the assumption of a linear model with additive noise, the maximum likelihood estimate of the information flow reads (Liang, 2021):

$$T_{j \to i} = \frac{1}{\det \mathbf{C}} \cdot \sum_{k=1}^{d} \Delta_{jk} C_{k,di} \cdot \frac{C_{ij}}{C_{ii}}, \tag{5}$$

where $T_{j \to i}$ is the absolute rate of information transfer from variable x_j to variable x_i, $\mathbf{C}$ is the covariance matrix, d is
195   the number of variables, Δ_{jk} are the cofactors of $\mathbf{C}$ ($\Delta_{jk} = (-1)^{j+k} M_{jk}$, where M_{jk} are the minors), $C_{k,di}$ is the sample covariance between all x_k and the Euler forward difference approximation of $\mathrm{d}x_i/\mathrm{d}t$, C_{ij} is the sample covariance between x_i and x_j, and C_{ii} is the sample variance of x_i. Note that a nonlinear version of LKIF has recently been developed but will not be used in this study (Pires et al., 2023).

To assess the importance of the different cause-effect relationships, we compute the relative rate of information transfer $\tau_{j \to i}$

200 from variable x_j to variable x_i following the normalization procedure of Liang (2015, 2021):

$$\tau_{j \to i} = \frac{T_{j \to i}}{Z_i}, \tag{6}$$

where Z_i is the normalizer, computed as follows:

$$Z_i = \sum_{k=1}^{d} |T_{k \to i}| + \left| \frac{dH_i^{noise}}{dt} \right|, \tag{7}$$

where the first term on the right-hand side represents the information flowing from all the x_k to x_i (including the influence

205 of x_i on itself), and the last term is the effect of noise (taking stochastic effects into account), computed following Liang (2015, 2021).

In the following, we will only use the relative rate of information transfer τ (expressed in %). When $\tau_{j \to i}$ is significantly different from 0, x_j has an influence on x_i, while if $\tau_{j \to i} = 0$ there is no influence. The absolute value of τ indicates the strength of the causal influence. A positive (negative) value is indicative of an increase (decrease) in variability of the target variable

210 x_i due to the causal influence of the source x_j. However, we will mainly use the absolute value of τ in this study, and will only briefly discuss the sign in the case of the Lorenz (1963) model (Fig. 7). Statistical significance of $\tau_{j \to i}$ is computed via bootstrap resampling with replacement of all terms included in Eq. (5)-(7) and using a significance level $\alpha = 5$ %. The number of bootstrap realizations varies depending on the case study: 100 for the 2D and Lorenz (1963) models, 300 for the 6D and 9D models, and 1000 for the real-case study. This number is chosen sufficiently large to achieve convergence of results.

215 ## 3.2 Peter and Clark momentary conditional independence (PCMCI)

The PCMCI method is a causal discovery method based on the Peter and Clark (PC) algorithm (Spirtes et al., 2001), combined with the momentary conditional independence (MCI) approach (Runge et al., 2019b). Given a set of univariate time series (called 'actors'), PCMCI estimates their causal graph representing the conditional dependencies among the time-lagged actors. In its linear application, PCMCI uses partial correlations to iteratively test conditional dependencies in a set of ac-

220 tors, distinguishing between true causal links and spurious links arising from autocorrelation effects, indirect links or common drivers.

Note that the term 'causal' rests upon a set of assumptions, such has (1) causal sufficiency, (2) causal Markov condition, (3) faithfulness, (4) instantaneous effects, (5) stationarity, (6) dependency type assumptions and (7) measurement error (see Runge (2018) for further details). In general, the causal graph should represent a stationary (stable in time) set of causal links,

225 in which causality is determined with a lag l of at least one time step and it is only true among the specific set of analysed actors. The PCMCI algorithm is composed of two steps, the PC-step and the MCI-step. Each step is briefly described in this section.

In the first step, or PC-step, for each actor in the (example) set of actors P, the algorithm identifies the initial set of parents P^0 based only on the simple correlation between each actor and all other actors up to a maximum lag l_{max}. Let us assume

230   that with $l_{max} = 3$, $P = \{A, B, C, D, E\}$ and $P_A^0 = \{A_{l=-1}, B_{l=-1}, D_{l=-2}, C_{l=-2}, E_{l=-1}\}$, where actors A to E in the set of parents of A, P_A^0, are ordered based on the absolute value of their correlation coefficient with $A_{l=0}$. Then, in the first iteration of the algorithm, the partial correlation ρ between $A_{l=0}$ and each actor in P_A^0 is calculated by conditioning on an additional actor taken from P_A^0. For example, ρ ($A_{l=0}$, $A_{l=-1}$ | $B_{l=-1}$) = ρ (Res($A_{l=0}$), Res($A_{l=-1}$)), where Res($A_{l=0}$) and Res($A_{l=-1}$) are the residuals of $A_{l=0}$ and $A_{l=-1}$ after removing the linear influence of $B_{l=-1}$. The partial correlation is computed for each

235   actor in P_A^0 by conditioning (only once) on the strongest available actor. At the end of this first iteration, the set of parents of A is updated. Let us assume that in our example, $P_A^1 = \{A_{l=-1}, B_{l=-1}, C_{l=-2}, E_{l=-1}\}$, then in the second iteration, the set of parents P_A^2 will be identified by conditioning on the first two strongest actors, e.g. ρ ($A_{l=0}$, $A_{l=-1}$ | $B_{l=-1}$, $C_{l=-2}$). The PC-step ends when the number of actors on which to condition equals the numbers of actors contained in P_A^n. Then, the same computation is repeated for each actor contained in P, until each actor has its own set of parents P_n.

240   In the second step, or MCI-step, the partial correlation between each possible pair of actors is calculated a second time by regressing once on the combined set of parents. If we assume that $P_A^4 = \{A_{l=-1}, C_{l=-2}, E_{l=-1}\}$ and $P_B^3 = \{B_{l=-1}, A_{l=-2}, D_{l=-1}\}$, then a causal link between $A_{l=0}$ and $B_{l=-1}$ is detected if their partial correlation conditioned on their joint set of parents is significant for a certain threshold α. In this example, ρ ($A_{l=0}$, $B_{l=-1}$ | $A_{l=-1}$, $C_{l=-2}$, $E_{l=-1}$, $B_{l=-2}$, $A_{l=-3}$, $D_{l=-2}$) (note that the lag of P_B^3 is increased accordingly). At the end of the MCI-step, each actor will have its own set of causal parents, and

245   the causal effect of each link can be computed.

   The strength of a causal link from variable x_j at time (t - l) to variable x_i at time t, noted $x_{j,t-l} \rightarrow x_{i,t}$, is expressed in terms of the path coefficient β, which measures the change in the expectation of $x_{i,t}$ following an increase of $x_{j,t-l}$ by one standard deviation, keeping all other parents of $x_{i,t}$ constant. The linear coefficients β are calculated as follows:

$$x_{i,t} = \sum_{k=1}^{N} \beta_k x_{j,k} + \eta_{x_i}, \tag{8}$$

250   where $x_{j,k} \in P\{x_i\}$ ($k =1,...,N$) is the set of parents of $x_{i,t}$ (N is the number of parents), and η_{x_i} is the residual of $x_{i,t}$. Like LKIF, PCMCI assumes that the system is linear, but a nonlinear version of the algorithm also exists (which has not been used for the present study).

3.3   Differences between the two methods

Before investigating results from the two causal methods, it is important to highlight the main differences between the two

255   methods, which are summarized in Table 1. LKIF is directly derived from the propagation of information entropy (Liang, 2016) and quantifies the rate of information transfer from one variable to the other (Liang, 2014, 2021). PCMCI, on the other hand, is a causal network algorithm starting with a fully connected graph from which non-causal links are iteratively removed based on conditioning sets of growing cardinality (Spirtes et al., 2001; Runge et al., 2019b).

   The metric used by LKIF is the rate of information transfer from variable x_j to variable x_i and can be expressed either in

260   nats per unit time (for T; Eq. (5)) or in percent (for τ; Eq. (6)). For PCMCI, the path coefficient β (Eq. (8)) measures the expected change in x_i at time t (in units of standard deviation) if x_j is perturbed at time $t - l$ by one standard deviation. While

time lags must be incorporated with PCMCI, LKIF has not been designed to work with such lags by default, although they can be used in principle (Liang et al., 2021).

While for both methods, the strength of the metric, in absolute value, indicates how strongly two variables are causally linked, i.e. the larger $|\tau|$ and $|\beta|$, the larger the causal link, the sign has a different meaning. For LKIF, a positive (negative) value of $\tau_{j \to i}$ means that the variability of the source x_j increases (decreases) the variability of the target x_i. For PCMCI, the sign of $\beta_{j \to i}$ is closely linked to the correlation between x_j and x_i, i.e. a positive (negative) value means that an increase in x_j leads to an increase (a decrease) in x_i in the subsequent time step.

Table 1. Main differences between the two causal methods used in this study.

	LKIF	PCMCI
Full name	Liang-Kleeman information flow	Peter and Clark momentary conditional independence
Type of method	Information flow	Causal discovery algorithm
Use of time lags	Not by default	Always
Use of iterative conditioning	No	Yes
Metric	Rate of information transfer T (absolute) or τ (relative)	Path coefficient β
Unit	T: nats time^{-1}; τ: %	No unit
Sign meaning	> 0: x_j variability → x_i variability ↑ < 0: x_j variability → x_i variability ↓	> 0 : x_j ↑→ x_i ↑ < 0 : x_j ↑→ x_i ↓
Key references	Liang (2014, 2021)	Spirtes et al. (2001); Runge et al. (2019b)

4 Results

We provide results from the four artificial models and the real-case study hereafter. Table 2 summarizes the occurrence of true-positive, false-positive and false-negative rates for the three first models and will be discussed in Sect. 5.1.

4.1 2D model

For the 2D model, the numerical value of the correlation between x_1 and x_2 is significantly positive ($R = 0.23$; Fig. 1(a)) and is similar to the analytical value (Fig. 1(d)), but it does not provide any indication on the direction of influence.

LKIF can accurately retrieve the correct causal link, i.e. from x_2 to x_1, as well as the absence of influence in the reverse direction (Fig. 1(b)), as was already demonstrated in Liang (2014). In addition, the numerical estimate of the rate of information transfer ($|\tau_{2 \to 1}| = 5.72$ %; Fig. 1(b)) is very close to the analytical solution ($|\tau_{2 \to 1}| = 5.56$ %; Fig. 1(e)), which provides confidence in the LKIF results found for this simple system.

PCMCI only captures the self-influences of x_1 and x_2, but is not able to capture any significant causal influence between x_1
280 and x_2 with the original time step, i.e. dt = 0.001 (Fig. 1(c)). This missed detection is partly due to the fact that PCMCI responds
better for discrete maps with finite time steps. Indeed, the time step for discretization is too small, and if we re-compute causal
links with PCMCI taking every 100 time steps (dt = 0.1), we can recover the influence from x_2 to x_1, although the value of β
is relatively small (Fig. 1(c)).

This example shows that LKIF performs well for such a very simple 2D system, while PCMCI does not.
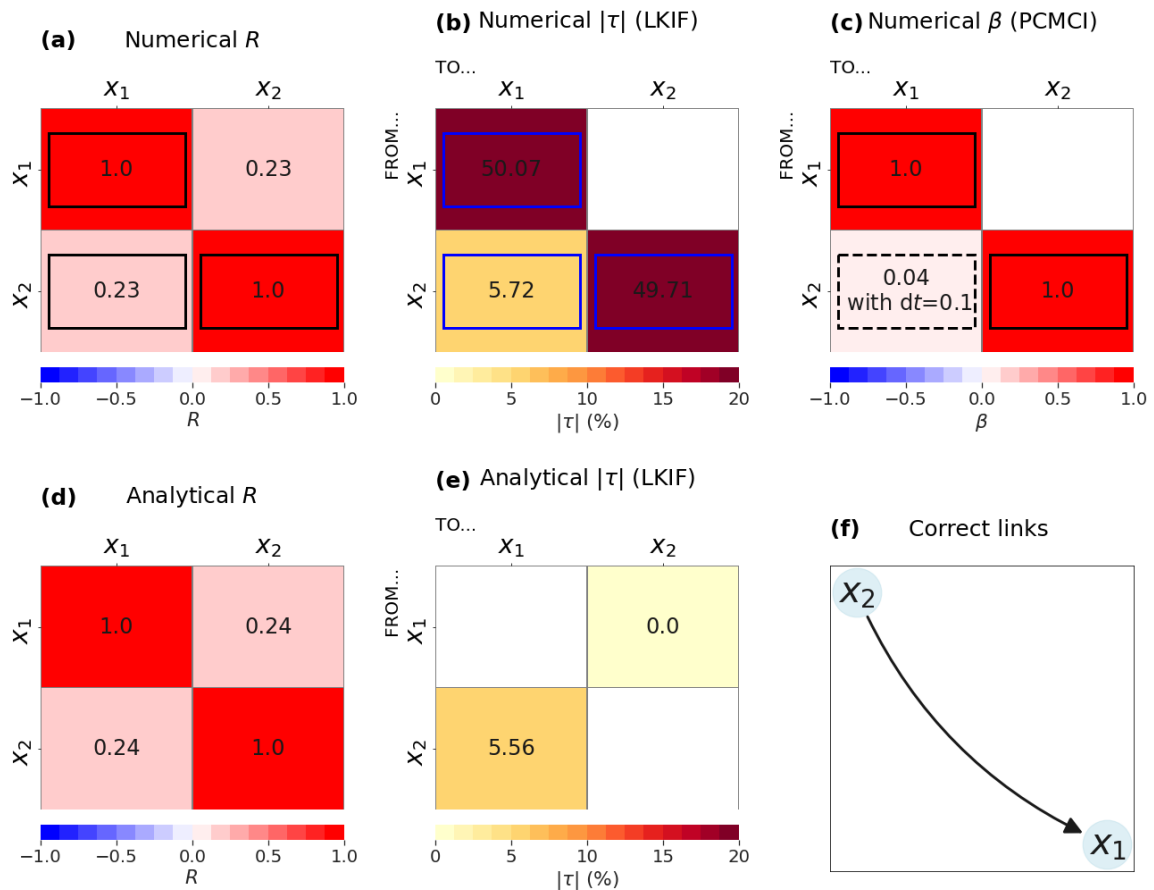
Figure 1. Numerical results from the 2D model: (a) correlation coefficient, (b) rate of information transfer (LKIF, absolute value), and (c)
maximum path coefficient (PCMCI) when using 3 lags (0 to 2 time steps). Analytical values of (d) correlation coefficient, and (e) rate of
information transfer (LKIF). (f) Correct causal links from Eq. (1). For numerical results, only significant values at the α = 5% level are
shown, and correct causal links are highlighted by black or blue contours. The dashed contour in panel (c) indicates a significant value with
a larger time step (dt = 0.1), while it is not significant with the original time step (dt = 0.001).

4.2 6D model

For the 6D model, the correlations are significant for all 30 pairs of variables (excluding auto-correlations), despite relatively small values for many of them (Fig. 2(a)). This shows that a simple correlation analysis fails to only identify the seven causal links that should be identified in this system (Fig. 2(d)). The largest correlation of all pairs is between x_2 and x_5 ($R = 0.37$), but no causal link should exist between the two variables (i.e. this is a false positive). This large correlation probably appears because x_6 influences both x_2 and x_5 by construction (Fig. 2(d)) and is thus a confounding variable. Correlations larger than 0.3 in absolute value appear for the two pairs x_6-x_2 and x_6-x_5 (Fig. 2(a)), which confirms the role of x_6 as a confounding variable, but these correlations do not indicate the direction of influences.

Both LKIF (Fig. 2(b); no lag is used) and PCMCI (Fig. 2(c); use of four time lags) can capture the seven correct causal links (Fig. 2(d)), i.e. the directed cycle $x_1 \rightarrow x_2 \rightarrow x_3 \rightarrow x_1$, the two-way causal link between x_4 and x_5, and the influence of x_6 on both x_2 and x_5. Results from PCMCI in terms of self-influences are more accurate based on Eq. (2), as it provides two significant self-influences, i.e. x_4 and x_6, while LKIF identifies all six self-influences as significant.

This example shows the strength of causal methods, which can capture the correct causal influences, while the correlation is not able to provide such information and cannot identify confounding variables and the direction of causality.

4.3 9D model

For the 9D model, the correlation does a poor job at identifying correct causal influences (Fig. 3(a)). In particular, the largest correlation is between x_8 and x_9, which is not a correct causal link by construction (Eq. (3)). As for the 6D model, this is due to the fact that x_7 should influence both variables (Fig. 4(d)). x_7 is indeed significantly correlated to both x_8 and x_9, but the causal direction is not identified by the correlation analysis.

Using LKIF without any lag shows that the method can detect all correct links, except $x_5 \rightarrow x_4$, although only four causal influences have a rate of information transfer $|\tau|$ larger than 1 % (Fig. 3(b)). These four influences are the ones that should appear at lag -1 (Fig. 4(d), i.e. $x_1 \rightarrow x_3$, $x_6 \rightarrow x_4$, $x_7 \rightarrow x_8$ and $x_7 \rightarrow x_9$. The method also wrongly identifies 13 causal influences, even if values of information transfer remain small.

The use of time lags up to $l = 3$ time steps with LKIF (we use 9 variables × 4 lags = 36 variables in total) allows to improve results (Fig. 4(b), where the maximum value of all lags is plotted). In particular, all nine correct causal links can now be identified with $|\tau| > 3$ %, except the influence of x_3 on x_1, which is significant but has a much smaller value ($|\tau| = 0.68$ %). Five additional causal influences are wrongly identified by the method with lags up to 3 time steps, but with relatively small values ($|\tau| < 0.4$ %).

Using PCMCI with lags up to $l = 4$ time steps also allows to correctly reproduce all causal links, except that it wrongly identifies four additional causal influences but with very small values (Fig. 4(c)). All self-influences are also correctly identified by the two methods.
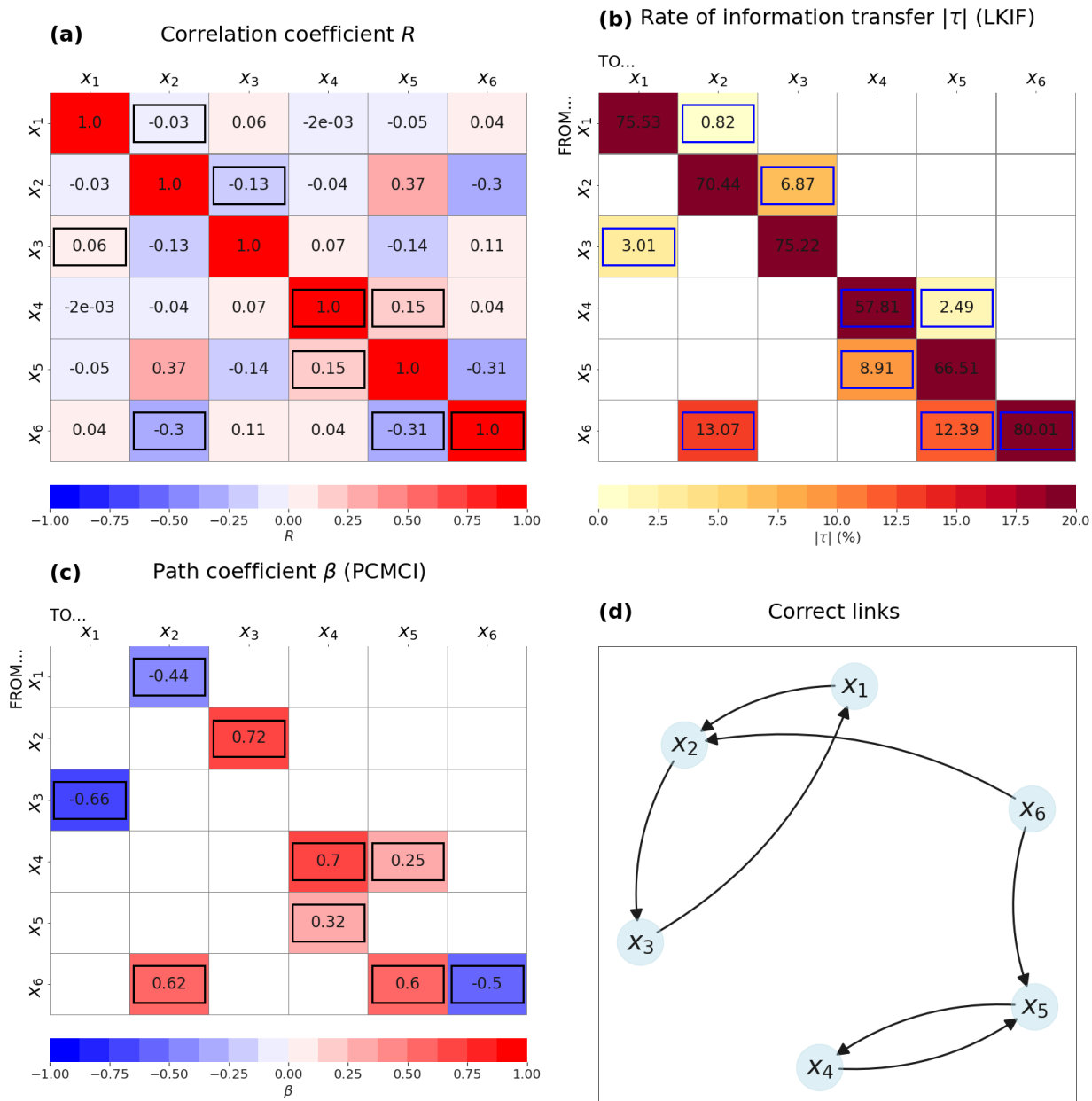
Figure 2. Results from the 6D model: (a) correlation coefficient, (b) rate of information transfer (LKIF, absolute value), and (c) maximum path coefficient (PCMCI) when using 4 lags (0 to 3 time steps). (d) Correct causal links from Eq. (2). Only significant values at the $\alpha = 5\%$ level are shown, and correct causal links are highlighted by black or blue contours.

This example also demonstrates the power of causal methods compared to a correlation analysis when using an appropriate number of lags: all expected links are correctly identified. Although some wrong causal links are identified by both methods, the strength of the relationship remains small for these wrong influences.
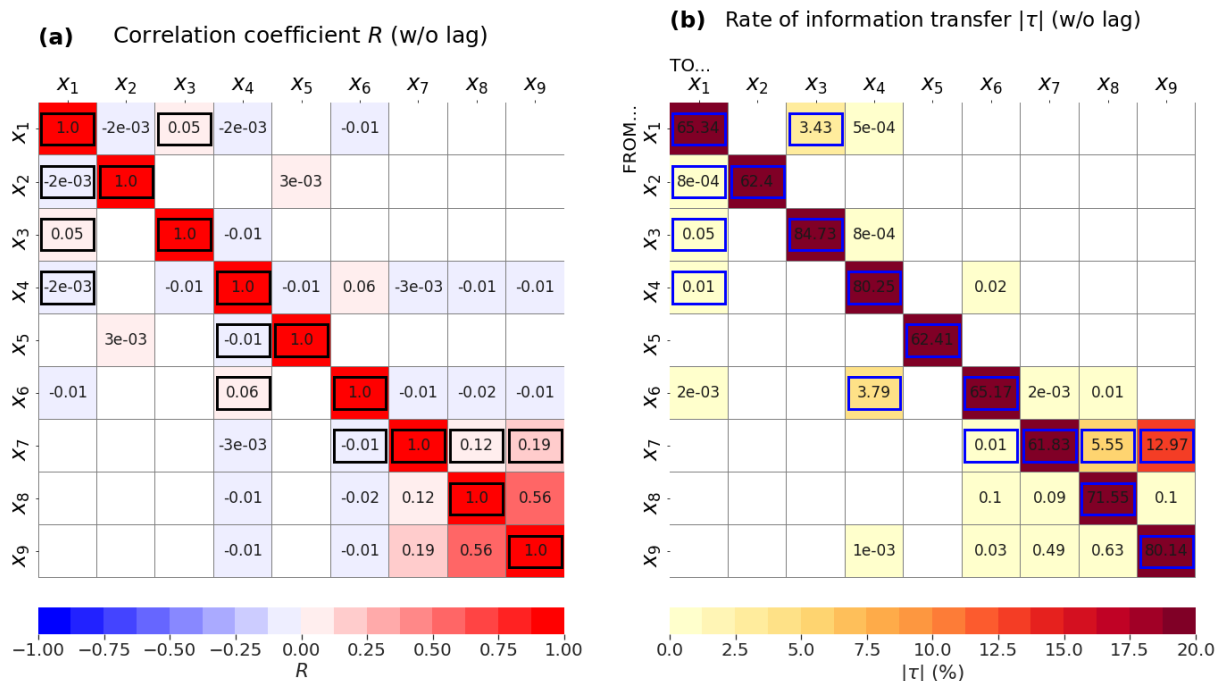
Figure 3. Results from the 9D model without lags: (a) correlation coefficient, and (b) rate of information transfer (LKIF, absolute value). Only significant values at the $\alpha = 5\%$ level are shown, and correct causal links are highlighted by black or blue contours.

4.4 Lorenz (1963) model

The only large correlation (excluding auto-correlation) in this system is between x and y, with $R = 0.88$ (Fig. 5(a)). The other correlations are very small ($R = -0.01$) but significant, probably due to the length of the time series.

According to LKIF, a two-way causal link appears between x and y (Fig. 5(b)). This causal link is also identified by PCMCI with lags up to $l = 3$ time steps (Fig. 5(c)). PCMCI also identifies a significant two-way causal link between y and z but the value is very close to 0.

Then, we investigate whether there is a lag dependence on the results. For the correlation and LKIF, we repeat the computation by shifting the three variables one by one with a lag from 0 to 1 unit time (100 time steps) with 0.1 unit time increment (i.e. every 10 time steps). For example, we take x_{t-l} at lag $l = 0.1$ unit time, and keep y_t and z_t at lag 0, and re-compute the correlation and relative rate of information transfer. Then, we take x_{t-l} at lag $l = 0.2$ unit time, keeping y_t and z_t at lag 0, and
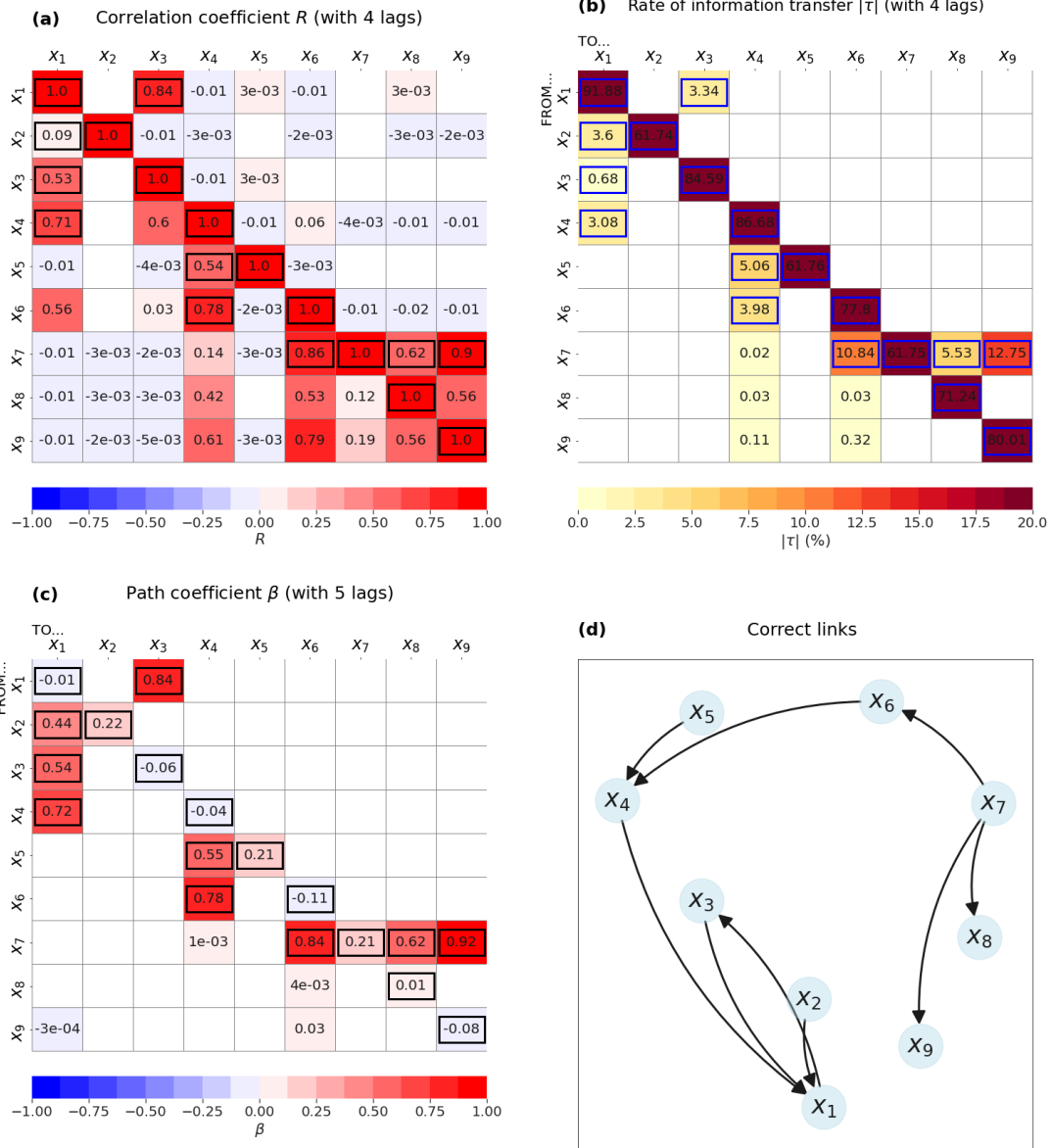
Figure 4. Results from the 9D model with lags: (a) maximum correlation coefficient when using 4 lags (0 to 3 time steps), (b) maximum rate of information transfer (LKIF, absolute value) when using 4 lags (0 to 3 time steps), (c) maximum path coefficient (PCMCI) using 5 lags (0 to 4 time steps). (d) Correct causal links from Eq. (3). Only significant values at the $\alpha = 5\%$ level are shown, and correct causal links are highlighted by black or blue contours.

so on until lag $l = 1$ unit time. We do the same when y leads x and z, and when z drives x and y. For PCMCI, all lags from 0 to

330   1 unit time with 0.01 unit time increment (i.e. every time step) are included in the same computation as the method is designed
to work with multiple lags by default. Results are presented in Fig. 6.

The correlation coefficient between x and y decreases exponentially with increasing lag when x leads y (Fig. 6(a)), and it
first increases from $l = 0$ to $l = 0.1$ unit time before decreasing exponentially when y leads x (Fig. 6(b)). No correlation appears
between z and any of the two other variables at any lag (Fig. 6(a)-(c)).

335   The LKIF rates of information transfer from x to y and from y to x also decrease with increasing lag between 0 and 1 unit
time, but starting with a plateau of $|\tau| \sim 50$ % (Fig. 6(d)-(e)). This plateau lasts from $l = 0$ to $l = 0.2$ unit time for $\tau_{x_{t-l} \rightarrow y_t}$
(Fig. 6(d)), and from $l = 0$ to $l = 0.4$ unit time for $\tau_{y_{t-l} \rightarrow x_t}$ (Fig. 6(e)). No information transfer exists between z and the two
other variables at any lag (Fig. 6(d)-(f)), in agreement with the absence of correlation (Fig. 6(a)-(c)).

The PCMCI path coefficients between x and y also generally decrease (in the two directions) with increasing lag, although
340   the decrease presents more variability than the correlation and LKIF, with $\beta = 0$ at lag 0, the largest β value when $l = 0.1$ unit
time, and then an oscillatory behavior until $l = 1$ unit time (Fig. 6(g)-(h)). As for the correlation and LKIF, no causal influence
is found between z and the two other variables at any lag (Fig. 6(g)-(i)).

If we replace x by x^2 to take nonlinearities into account and look at the triplet (x^2, y, z), a strong positive correlation now
appears between x^2 and z ($R = 0.65$; Fig. 5(d)). In addition, a strong two-way causal link now appears between x^2 and z with
345   both LKIF ($|\tau| \sim 50$ % in the two directions; Fig. 5(e)) and PCMCI ($|\beta| = 1.7$ in the two directions; Fig. 5(f)). This shows that
the linear versions of LKIF and PCMCI can detect causal links between nonlinear variable changes in nonlinear models. In
this case, the correlation between x and y, combined with the nonlinear forcing product xy in the third equation of the Lorenz
(1963) model (z equation; Eq. (4)), results into a linear correlation between z and the nonlinear non-invertible variable change
x^2.

350   The correlation between x^2_{t+l} and z_t oscillates between $R \sim$ -0.7 ($l = 0.2$ unit time) and $R \sim 0.9$ ($l = $ -0.1 unit time) with
a period of ~ 0.7 unit time (Fig. 7(a)). The rates of information transfer from x^2_{t+l} to z_t and from z_t to x^2_{t+l} also show an
oscillatory behavior with a period of ~ 0.35 unit time (Fig. 7(b)), that is the half of the correlation oscillation. PCMCI does not
exhibit such an oscillatory behavior but rather a quickly decreasing β value for small lags (Fig. 7(c)).

4.5   Climate indices

355   The real-case study with climate indices shows that 54 % of the pairs of variables (excluding auto-correlations) are related
by significant correlations when considering no lag (Fig. 8(a)). However, it is obvious that a large number of these pairs are
correlated but not causally linked. The use of causal methods allows to remove such spurious links, as demonstrated by the
application of LKIF without any lag (Fig. 8(b)) and PCMCI with lags up to $l = 2$ months (Fig. 8(c)).

Results from the two causal methods present several similarities, including the AO influence on both PDO and TNA
360   (Fig. 8(b)-(c)). Another similarity is the two-way causal link between AMO and TNA, in agreement with Vannitsem and
Liang (2022) and Silini et al. (2022). The AMO-TNA influence is not surprising as both indices are computed from SST
anomalies in the North Atlantic, with AMO spanning the majority of the North Atlantic and TNA focusing on the tropical
region. Values of the AMO-TNA influence in the two directions are relatively strong for LKIF ($|\tau_{AMO \rightarrow TNA}| = 22$ % and
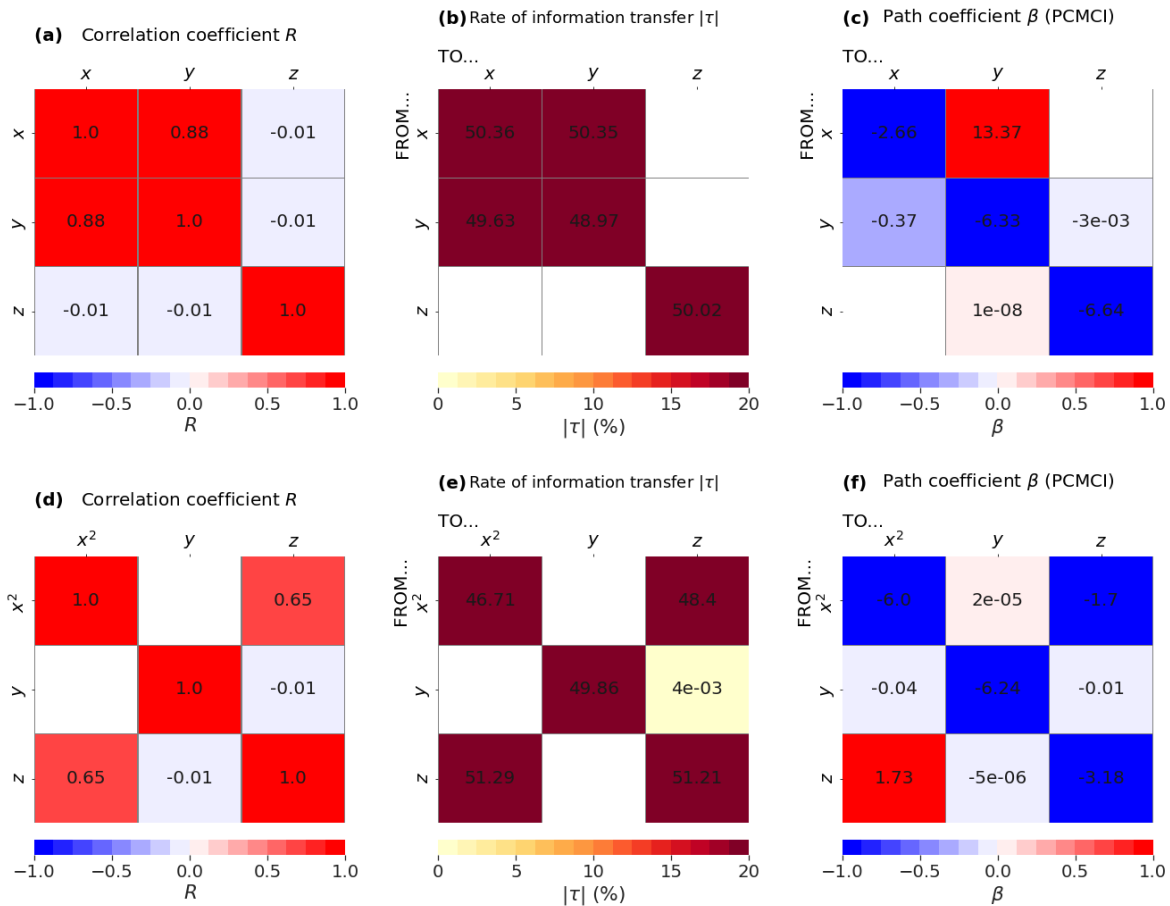
Figure 5. Results from the Lorenz (1963) model when using (x,y,z): (a) correlation coefficient, (b) rate of information transfer (LKIF, absolute value), and (c) maximum path coefficient (PCMCI) when using 4 lags (0 to 3 time steps). Results from the Lorenz (1963) model when using (x^2,y,z): (d) correlation coefficient, (e) rate of information transfer (LKIF, absolute value), and (c) maximum path coefficient (PCMCI) when using 4 lags (0 to 3 time steps). Only significant values at the $\alpha = 5\%$ level are shown.

$|\tau_{TNA \rightarrow AMO}| = 38$ %) compared to other pairs of influence (Fig. 8(b)). In addition, ENSO influences PDO according to both
365 methods (Fig. 8(b)-(c)), and the positive sign of the correlation means that a warm Niño3.4 phase results in a positive PDO
(Fig. 8(a)). The ENSO influence on PDO was recently reported by Vannitsem and Liang (2022), also using LKIF, and Silini
et al. (2022), based on the pseudo-transfer entropy. Spatial patterns of ENSO and PDO are very similar and PDO is often being
viewed as ENSO-like interdecadal climate variability, with PDO occuring at decadal time scale, while ENSO is predominantly
an interannual phenomenon (Mantua et al., 1997; Zhang et al., 1997).
370   In terms of differences between the two causal methods, LKIF identifies additional causal influences of AO on PNA, NAO
and AMO, while PCMCI does not identify these causal links (Fig. 8(b)-(c)). It is well known that there is a clear relationship
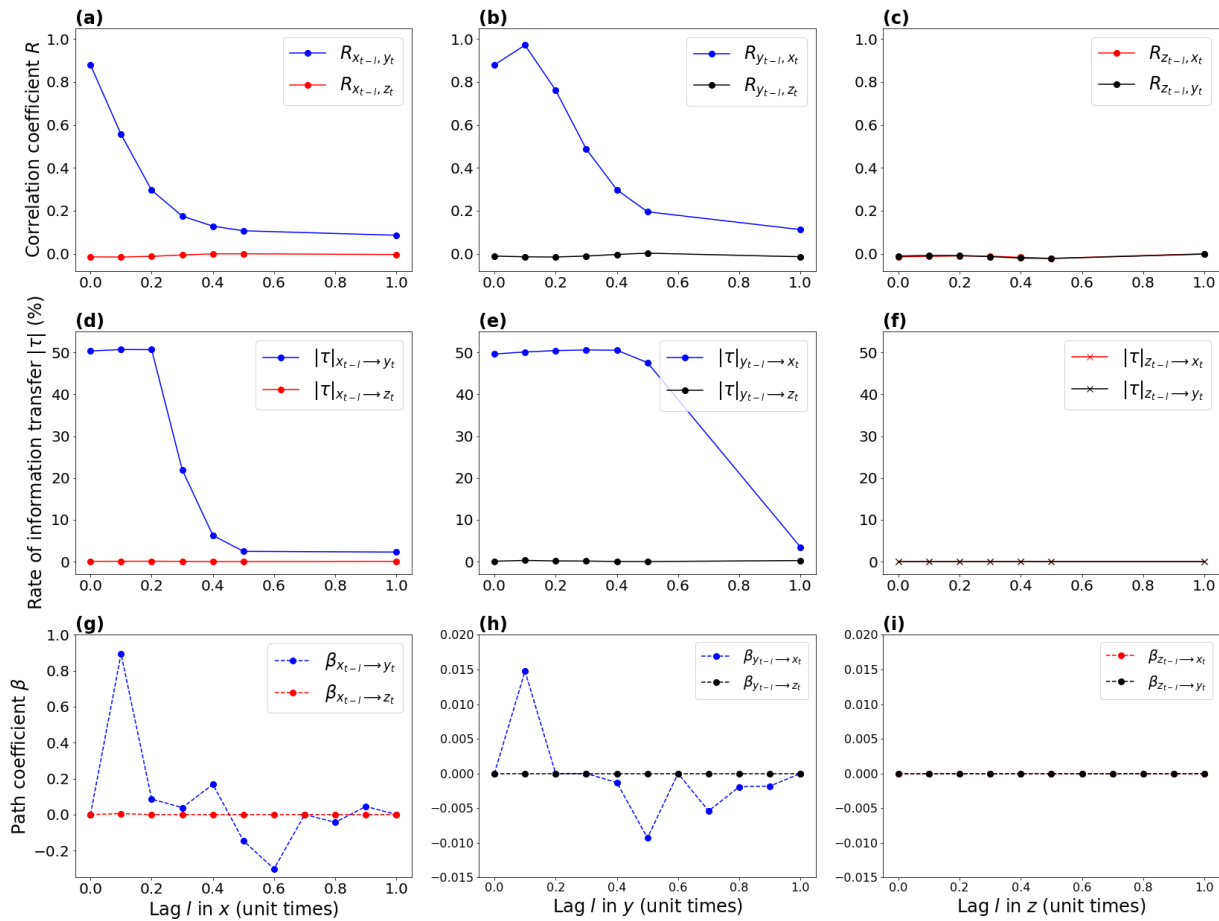
Figure 6. Results from the Lorenz (1963) model when using (x,y,z): (a)-(c) correlation coefficient, (d-f) rate of information transfer (LKIF, absolute value), and (g-i) path coefficient (PCMCI) as a function of the lag l when (a),(d),(g) x leads, (b),(e),(h) y leads, and (c),(f),(i) z leads.

between AO and NAO (Deser, 2000), and NAO is often referred to as the local manifestation of the AO (Hamouda et al., 2021). Also, according to LKIF, there are two-way causal influences between ENSO and PNA and between ENSO and TNA, which do not appear with PCMCI with lags up to $l = 2$ months (Fig. 8(b)-(c)). It is well know that ENSO has a major influence

375   on the extratropical Northern Hemisphere climate variability, in particular on PNA (Horel and Wallace, 1981). However, the influence of ENSO on PNA is complicated by the fact that other mechanisms can affect this relationship, such as the position of the Pacific jet stream (Soulard et al., 2019). Our results with LKIF suggest that PNA has a stronger influence on ENSO than the reverse, which would go in favor of more complex mechanisms in action. Finally, the influence of ENSO on TNA has also been reported in the literature and different mechanisms have been proposed (García-Serrano et al., 2017). It is interesting to

380   find that the influence of TNA on ENSO is stronger than the reverse influence with LKIF (Fig. 8(b)).
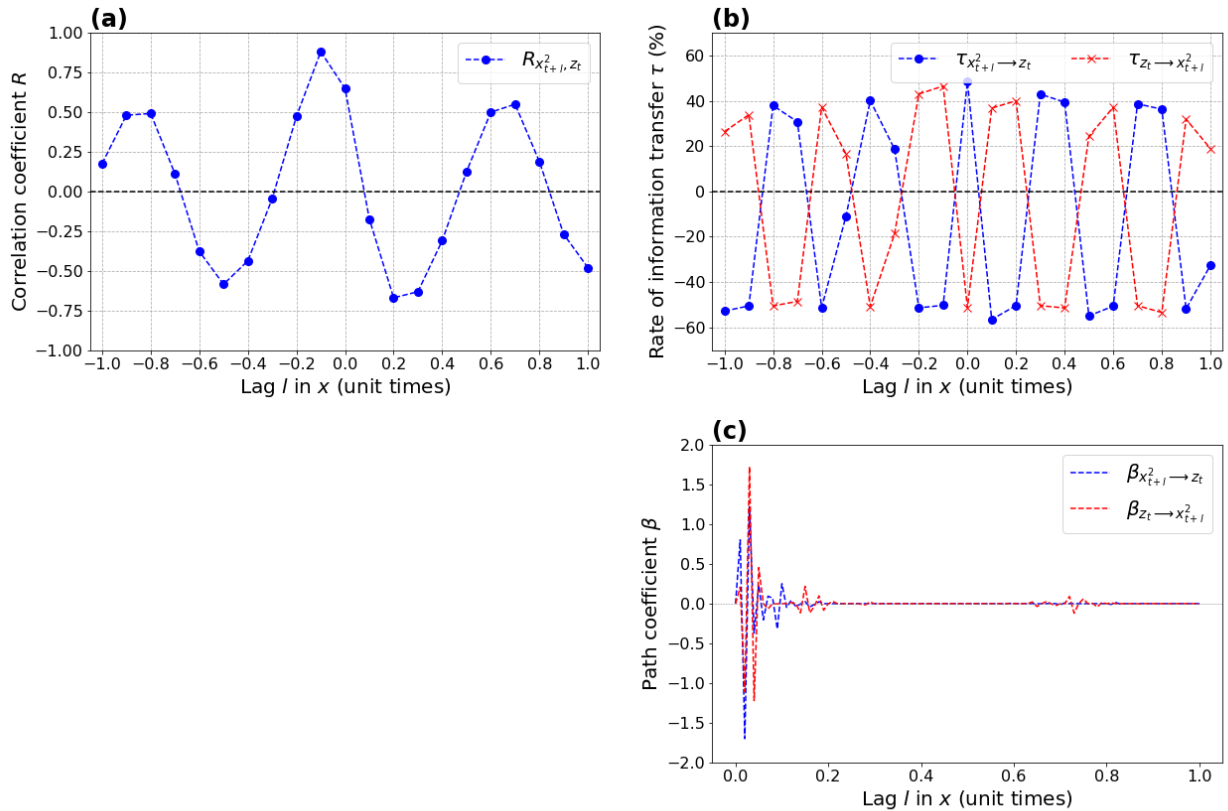
Figure 7. Results from the Lorenz (1963) model when using (x^2, y, z): (a) correlation coefficient, (b) rate of information transfer (LKIF), and (c) path coefficient (PCMCI) as a function of the lag l in x.

The use of 12 time lags (0 to 11 months) with both methods (bringing 8 variables × 12 lags = 96 variables in total for LKIF) provides additional insights (Figs. 9-10). PNA influences ENSO with a 1-month lag with LKIF (Fig. 9(a)), and with a 4-month lag with PCMCI (Fig. 10(a)). Additionally, PNA influences PDO with a 4-month lag and AMO with a 11-month lag using LKIF (Fig. 9(a)). However, all PNA influences appear relatively weak in intensity ($|\tau| < 1$ % with LKIF and $|\beta| < 0.1$).

385   NAO influences PDO with both methods but with very different lags depending on the method, i.e. 11 months with LKIF (Fig. 9(b)) and 1 month with PCMCI (Fig. 10(b)). It also influences TNA with LKIF with a 1-month lag. As for PNA, all significant NAO influences remain limited in intensity ($|\tau| < 1$ % with LKIF and $|\beta| < 0.1$).

AO is by far the climate index that influences most variables with LKIF (Fig. 9(c)), in agreement with Vannitsem and Liang (2022). When considering no lag, AO influences all other indices, except QBO and ENSO (Fig. 9(c)). The largest value of

390   rate of information transfer is from AO to NAO with $|\tau| = 4$ %, in agreement with the value considering no lag (Fig. 8(b)). AO also influences TNA and AMO at larger lags with LKIF ($l = 1$, 2 and 4 months for TNA, and $l = 2$, 5 and 11 months for

AMO). With PCMCI, AO only influences TNA at lags $l = 1$ to 4 months, PDO at lag $l = 1$ month, and QBO at lag $l = 4$ months (Fig. 10(c)). It is intriguing to notice that no AO influence on NAO appears with PCMCI.

QBO does not have any influence on any other climate indices with any of the methods (Figs. 9(d) and 10(d)).

395 The AMO-TNA two-way causal influence already identified in Fig. 8 also appears in the lagged plots, however with contrasting behaviors depending on the causal method. With LKIF, AMO only influences TNA at lag 0 (Fig. 9(e)) and TNA influences AMO at lags $l = 0$ and 11 months (Fig. 9(g)). With PCMCI, the AMO influence on TNA increases with increasing lag from $l = 0$ to 6 months, then decreases and stays relatively constant until $l = 11$ months (Fig. 10(e)), and TNA influences AMO at lags $l = 2$, 4-6, 8 and 10-11 months (Fig. 10(g)). TNA has additional influences with PCMCI at lags $l \geq 2$ months (on NAO,

400 QBO, PDO and ENSO; Fig. 10(g)) and with LKIF at lags $l \geq 9$ months (on PDO and ENSO). The TNA influences on PDO and ENSO, appearing for both causal methods, remain limited to large lags (Figs. 9(g)- 10(g)).

PDO has an influence on PNA with LKIF at lag $l = 6$ months (Fig. 9(f)), which is consistent with Simon et al. (2022) using sensitivity experiments with a coupled model. According to PCMCI, PDO influences ENSO at lags $l \geq 3$ months (Fig. 10(f)).

Finally, ENSO influences PDO at lags $l = 0$, 2 and 6 months, and influences TNA at lags $l = 2$ and 6 months with LKIF

405 (Fig. 9(h)). With PCMCI, ENSO is the climate index that influences most variables (all but NAO), especially PDO from $l = 2$ to 10 months, TNA from $l = 3$ to 11 months, and AMO from $l = 4$ to 11 months (Fig. 10(h)). The large role of ENSO was also reported using the pseudo-transfer entropy using lags $l = 1$ to 9 months (Silini et al., 2022).

5 Discussion

Correlation is often used by the climate community to identify potential relationships between variables, but a statistically

410 significant correlation does not necessarily imply causation. In our study, we used two causal methods, LKIF and PCMCI, to disentangle true causal links from spurious correlations, and applied them to four artificial models and one real-case study based on climate indices. Below we discuss our results compared to previous literature (Sect. 5.1 for the artificial models and Sect. 5.2 for the real-case study).

5.1 Artificial models

415 For the simplest (2D) model used here, we show that LKIF can accurately reproduce the correct causal link, with relatively high accuracy compared to the analytical solution, while PCMCI fails to reproduce this link when using the original time step (Sect. 4.1 and Fig. 1). PCMCI provides the correct influence for the 2D model when taking every 100 time steps (although the β value is small), which shows that PCMCI responds better for discrete maps with finite time steps. For the 6D model, both LKIF and PCMCI can detect the correct causal links (Sect. 4.2 and Fig. 2). For the 9D nonlinear model, PCMCI allows to retrieve

420 the correct causal relationships, while some care with the number of lags is needed with LKIF to achieve appropriate results (Sect. 4.3 and Figs. 3-4). This shows that LKIF performs better for simpler systems and presents a bit more difficulties with more complex models with several lags, while PCMCI is better with models having more variables and several lags. Results from the Lorenz (1963) model are more complicated to interpret as the system is highly nonlinear and chaotic. Both methods
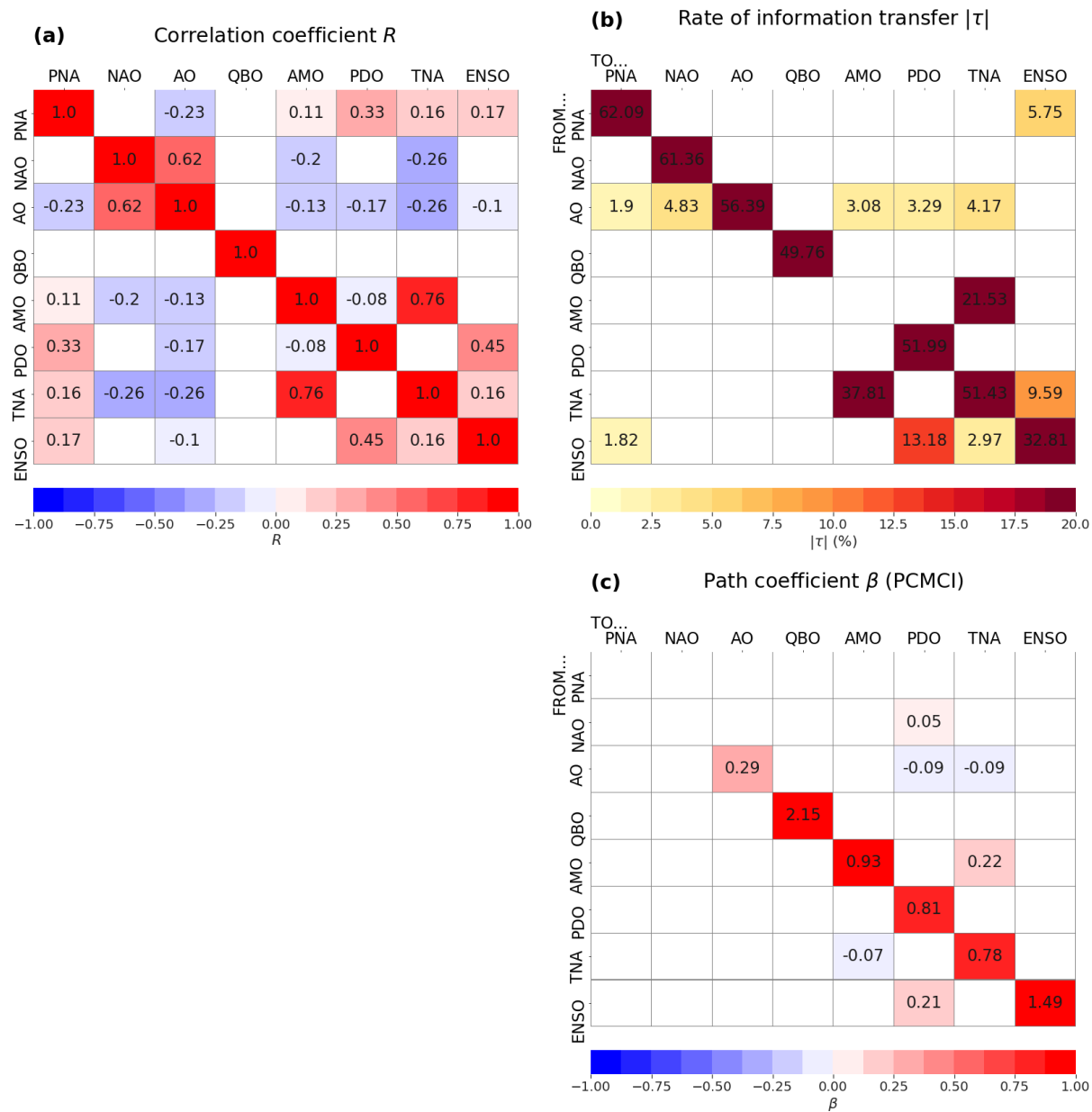
Figure 8. Results from the real-case study: (a) correlation coefficient, (b) rate of information transfer (LKIF, absolute value), and (c) maximum path coefficient (PCMCI) when using 3 lags (0 to 2 months). Only significant values at the $\alpha = 5\%$ level are shown.

detect the same causal links (Sect. 4.4 and Fig. 5), although some differences appear in the dependence of the causal influence

425 on the time lag (Figs. 6-7). Moreover, the combination of model nonlinearities and nonlinear variable changes can result into linear causal links detectable by LKIF and PCMCI (Fig. 5).

The above results are not entirely comparable to findings from Krakovská et al. (2018) from a methodological perspective, as the latter used other causal methods and different coupled systems. However, a similarity is the fact that some methods (Granger causality and its extensions) better perform with the simplest models, while other methods (CCM and predictability

430 improvement) are better suited for more complex systems (Krakovská et al., 2018). This goes in hand with LKIF being better with the 2D model and PCMCI well suited for the 9D model in our analysis. Thus, the key finding from Krakovská et al. (2018) that 'it is important to choose the right method for a particular type of data' is also valid for our study.

The main novelties compared to Krakovská et al. (2018) are that: (1) we use two causal methods that had not been compared yet; (2) we compare our causal methods to the classical correlation coefficient; (3) we assess causality between nonlinear

435 variable changes and (4) we apply the two methods to a real-case study. Regarding (1), no definite conclusion can be provided as to which method is the best: it depends on the data type used. For a very simple model, like the 2D model, LKIF should be privileged over PCMCI. For a more complex model involving more variables and several lags, like the 9D model, PCMCI is better suited. In any case, we recommend to use as many methods as possible for a specific problem to increase the robustness of results. Regarding (2), we show that both LKIF and PCMCI are superior to correlation, as they allow to remove spurious

440 links. Regarding (3), we show that the combination of model nonlinearities with nonlinear variable changes can result into linear causal links, detectable by both LKIF or PCMCI. Point (4) is discussed in Sect. 5.2.

Table 2 provides true-positive, false-positive and false-negative rates for the correlation and the two causal methods used in this study and for the three first artificial models (2D, 6D and 9D models). For the 9D model, a distinction is made between the case where lags are not considered (PCMCI is not used in this case) and the case where lags are considered. These diagnostics

445 are not computed for the Lorenz (1963) model and the real-case study, as no exact solution exists for these two cases. Results show that the correlation has a large chance of detecting false positives (i.e. incorrect detection of causal influences) for all models, that LKIF performs better for the 2D and 6D models (as well as the 9D model with inclusion of lags), and that PCMCI is better suited for the 6D and 9D models (as well as the 2D model with an appropriate time step).

5.2 Climate indices

450 In our study, we extend previous analyses from Vannitsem and Liang (2022) and Silini et al. (2022) by using monthly time series of climate indices in the North Atlantic and North Pacific. We use the same seven climate indices as Vannitsem and Liang (2022), add QBO to the list to have four atmospheric and four oceanic indices, and do not use local air temperature, precipitation and insolation. Vannitsem and Liang (2022) also computed LKIF based on these indices but focused on the dependence of the rate of information transfer on the time scale (using a time-moving window) and did not compare LKIF

455 to another method. Silini et al. (2022) also used NAO, QBO, AMO, PDO and ENSO (Niño3.4), they used a slightly different index for TNA, and they incorporated 7 additional indices. The causal method used by Silini et al. (2022) is the pseudo-transfer entropy (Silini and Masoller, 2021).

Table 2. True-positive, false-positive and false-negative rates (in %) for the correlation and the two causal methods (LKIF and PCMCI) and for the first three artificial models (2D, 6D and 9D models, the latter without and with lags), excluding self-influences. The true-positive rate is the percentage of causal links correctly detected by the method among the total number of ground truth correct links (the latter is indicated in parentheses in the table). The false-positive rate represents the percentage of cases where the method incorrectly detects a causal link among the total number of ground truth incorrect links. The false-negative rate represents the percentage of cases where the method fails to find an existing causal link among the total number of ground truth correct links. For the 2D model and PCMCI, numbers are also provided in parentheses for the case with larger sampling time step ($dt = 0.1$).

		Correlation	LKIF	PCMCI
2D model	True positives (1)	100	100	0 (100)
	False positives	100	0	0 (0)
	False negatives	0	0	100 (0)
6D model	True positives (7)	100	100	100
	False positives	100	0	0
	False negatives	0	0	0
9D model without lag	True positives (9)	100	89	-
	False positives	40	21	-
	False negatives	0	11	-
9D model with lags	True positives (9)	100	100	100
	False positives	73	8	6
	False negatives	0	0	0

Due to the small methodological differences in our analysis compared to Vannitsem and Liang (2022) (see above), some small differences appear but key results with LKIF remain similar. In particular, we find that AO is the largest driver of all variables as it influences all other indices, except QBO and ENSO (Sect. 4.5 and Fig. 8(b)). We show that the AO influence mainly occurs at lag $l = 0$ (Fig. 9(c)). This is in agreement with Vannitsem and Liang (2022), who find that AO plays a key role at short time scale. PCMCI only identifies two AO influences with lags shorter than 2 months, i.e. to PDO and TNA (Fig. 10(c)). It is particularly intriguing to see that PCMCI does not detect the AO influence on NAO (Fig. 8(c)), while LKIF does (Fig. 8(b)), as NAO is often referred to as the local manifestation of AO (Hamouda et al., 2021). This discrepancy might hide seasonal differences, as for example winter and summer NAO have different spatial patterns (Folland et al., 2009).

ENSO is another climate index that has a relatively large influence on other climate indices, especially on PDO for both LKIF and PCMCI (Fig. 8(b)-(c)). The pivotal role of ENSO was already identified by Silini et al. (2022) and is not surprising due to its importance on the global climate (Timmermann et al., 2018). ENSO has a clear influence on PDO at lags 2 to 10 months for PCMCI (Fig. 10(h)), while it only appears at lags 0, 2 and 6 months for LKIF (Fig. 9(h)). This ENSO-PDO influence was detected from lags 1 to 7 with pseudo-transfer entropy (Silini et al., 2022), thus somewhere in between PCMCI and LKIF. The

other clear ENSO influence according to PCMCI, LKIF and pseudo-transfer entropy is on TNA, at lags 2 and 6 months with LKIF (Fig. 9(h)), at lags 3-11 months with PCMCI (Fig. 10(h)), and at lags 1-9 months with pseudo-transfer entropy (Silini et al., 2022). According to PCMCI and pseudo-transfer entropy, ENSO also largely influences other climate indices than PDO and TNA at different lags, which is not the case of LKIF. More research would be needed to further investigate this difference

475   between causal methods.

6   Conclusions

In this study, we compare two independent causal methods together, namely the Liang-Kleeman information flow (LKIF) and the Peter and Clark momentary conditional independence (PCMCI), and against the Pearson correlation coefficient. We use five different datasets with an increasing level of complexity, including three stochastic models, one nonlinear deterministic

480   model and one real-case study.

We show that both causal methods are superior to the correlation, which suffers from five key limitations: random coincidence, no identification of the direction of causality, external drivers not distinguished from direct drivers, no identification of potential nonlinear influences, and application to bivariate cases only. For most models and the real-case study, the number of significant correlations is much larger than the number of significant causal links, which is incorrect from a causal perspective

485   for the three first models. By extension, we assume that the correlation also suffers from this overestimation in the real-case study, and causal methods allow to improve results.

When comparing both causal methods together, LKIF can accurately reproduce the correct causal link in the 2D model, while PCMCI cannot with the original time step and needs to to be computed with a larger sampling time step to provide correct causal links, although the influence remains small. For the 6D model, both methods can capture the seven correct causal links.

490   For the 9D model, PCMCI correctly reproduces all causal links and LKIF without any time lag is not totally accurate. When used with time lags, LKIF can identify the correct causal links.

For the Lorenz (1963) model, results are more complicated to interpret as the system is highly nonlinear and chaotic. Both causal methods show a strong two-way causal link between x and y, while no causal link appears between z and the two other variables. However, when we replace x by x^2 to take nonlinearities into account, x^2 and z are causally linked (in the two

495   directions) with both methods. We also show that both LKIF and PCMI display a decrease in the two-way causal influence between x and y with increasing time lag, although the shape of this decrease is different between methods. Additionally, the oscillatory behavior in correlation coefficient and LKIF for the x^2-z pair as a function of lag is not displayed by PCMCI.

Finally, the real-case study with climate indices provides some similarities but also important differences between the two methods. In terms of similarities, AO influences both PDO and TNA, there is a two-way causal link between AMO and TNA, and ENSO influences PDO. In terms of differences, LKIF identifies additional influences of AO on PNA, NAO and AMO, as well as two-way causal links between ENSO and PNA, and between ENSO and TNA. When using 12 time lags, the number of influences detected by PCMCI becomes larger compared to LKIF, e.g. ENSO has a large influence on all other variables except

NAO, while AO remains the largest influencer (at smaller lags) with LKIF. More detailed analysis of the physical processes would be needed to identify correct causal links between these climate indices.

505   In summary, this analysis shows that both causal methods should be preferred to correlation when it comes to identify causal links. Additionally, as both LKIF and PCMCI display strengths and weaknesses when used with relatively simple models in which correct causal links can be detected by construction, we do not recommend one or the other method, but rather encourage the climate community to use several methods whenever possible. We finally highlight that both methods, as used here, assume linearity, so results need to be taken with caution for nonlinear problems, such as the Lorenz (1963) system and the real-case

510   study. The use of extensions of the methods for which fully nonlinear terms are taken into account are necessary to complement the current results (e.g. Pires et al. (2023)). Also, both LKIF and PCMCI deal with direct causal links, while other methods, such as interventional causality (Baldovin et al., 2020), can detect indirect influences. Further analysis would be needed to explore this aspect.

Code and data availability. The climate indices were retrieved on 20/01/2023 from the Physical Sciences Laboratory (PSL) of the National

515   Oceanic and Atmospheric Administration (NOAA; https://psl.noaa.gov/data/climateindices/list/). The Python scripts to produce the outputs and figures of this article, including the computation of LKIF, are available on Zenodo: https://zenodo.org/record/8383534 (Docquier, 2023).

Author contributions. DD, GDC, RVD, CALP, AS and SV designed the study. DD generated the model datasets and retrieved the climate indices. DD computed the LKIF method and Pearson correlation onto the datasets, and GDC run the PCMCI algorithm. DD led the writing of the manuscript, with contributions from all co-authors. DD created all figures, with the help of GDC. All authors participated to the data

520   analysis and interpretation.

Competing interests. Two of the co-authors (SV and RVD) are members of the editorial board of Nonlinear Processes in Geophysics. The authors have no other competing interests to declare.

Acknowledgements. We thank X. San Liang for his feedback related to our analysis. David Docquier, Giorgia Di Capua, Reik Donner, Carlos Pires, Amélie Simon and Stéphane Vannitsem were supported by ROADMAP (Role of ocean dynamics and Ocean-Atmosphere

525   interactions in Driving cliMAte variations and future Projections of impact-relevant extreme events; https://jpi-climate.eu/project/roadmap/), a coordinated JPI-Climate/JPI-Oceans project. David Docquier and Stéphane Vannitsem received funding from the Belgian Federal Science Policy Office under contract B2/20E/P1/ROADMAP. Giorgia Di Capua and Reik Donner were supported by the German Federal Ministry for Education and Research (BMBF) via the ROADMAP project (grant no. 01LP2002B). Carlos Pires is supported by Portuguese 'Ministry of Science, Technology and Higher Education' and 'Fundação para a Ciência e a Tecnologia' (FCT) I.P./MCTES through national funds

530   (PIDDAC) UIDB/50019/2020.

References

Årthun, M., Eldevik, T., Smedsrud, L. H., Skagseth, Ø., and Ingvaldsen, R. B.: Quantifying the influence of Atlantic heat on Barents Sea ice variability and retreat, Journal of Climate, 25, 4736–4743, https://doi.org/10.1175/JCLI-D-11-00466.1, 2012.

Bach, E., Motesharrei, S., Kalnay, E., and Ruiz-Barradas, A.: Local atmosphere-ocean predictability: Dynamical origins, lead times, and seasonality, Journal of Climate, 32, 7507–7519, https://doi.org/10.1175/JCLI-D-18-0817.1, 2019.

Baldovin, M., Cecconi, F., and Vulpiani, A.: Understanding causation via correlations and linear response theory, Physical Review Research, 2, 043 436, https://doi.org/10.1103/PhysRevResearch.2.043436, 2020.

Bishop, S. P., Small, R. J., Bryan, F. O., and Tomas, R. A.: Scale dependence of midlatitude air-sea interaction, Journal of Climate, 30, 8207–8221, https://doi.org/10.1175/JCLI-D-17-0159.1, 2017.

Coufal, D., Jakubík, J., Jacjay, N., Hlinka, J., Krakovská, A., and Paluš, M.: Detection of coupling delay: A problem not yet solved, Chaos, 27, 083 109, https://doi.org/10.1063/1.4997757, 2017.

Deser, C.: On the teleconnectivity of the "Arctic Oscillation", Geophysical Research Letters, 27, 779–782, https://doi.org/10.1029/1999GL010945, 2000.

Di Capua, G., Kretschmer, M., Donner, R. V., van den Hurk, B., Vellore, R., Krishnan, R., and Coumou, D.: Tropical and mid-latitude teleconnections interactingwith the Indian summer monsoon rainfall: a theory-guided causal effect network approach, Earth System Dynamics, 11, 17–34, https://doi.org/10.5194/esd-11-17-2020, 2020a.

Di Capua, G., Runge, J., Donner, R. V., van den Hurk, B., Turner, A. G., Vellore, R., Krishnan, R., and Coumou, D.: Dominant patterns of interaction between the tropics and mid-latitudes in boreal summer: causal relationships and the role of timescales, Weather and Climate Dynamics, 1, 519–539, https://doi.org/10.5194/wcd-1-519-2020, 2020b.

Docquier, D.: Codes to compute Liang index and correlation for comparison study, Zenodo, https://doi.org/10.5281/zenodo.8383534, 2023.

Docquier, D., Grist, J. P., Roberts, M. J., Roberts, C. D., Semmler, T., Ponsoni, L., Massonnet, F., Sidorenko, D., Sein, D. V., Iovino, D., Bellucci, A., and Fichefet, T.: Impact of model resolution on Arctic sea ice and North Atlantic Ocean heat transport, Climate Dynamics, 53, 4989–5017, https://doi.org/10.1007/s00382-019-04840-y, 2019.

Docquier, D., Vannitsem, S., Ragone, F., Wyser, K., and Liang, X. S.: Causal links between Arctic sea ice and its potential drivers based on the rate of information transfer, Geophysical Research Letters, 49, e2021GL095 892, https://doi.org/10.1029/2021GL095892, 2022.

Docquier, D., Vannitsem, S., and Bellucci, A.: The rate of information transfer as a measure of ocean-atmosphere interactions, Earth System Dynamics, 14, 577–591, https://doi.org/10.5194/esd-14-577-2023, 2023.

Enfield, D. B., Mestas-Nuñez, A. M., Mayer, D. A., and Cid-Serrano, L.: How ubiquitous is the dipole relationship in tropical Atlantic sea surface temperatures?, Journal of Geophysical Research, 104, 7841–7848, https://doi.org/10.1029/1998JC900109, 1999.

Enfield, D. B., Mestas-Nuñez, A. M., and Trimble, P. J.: The Atlantic Multidecadal Oscillation and its relation to rainfall and river flows in the continental U.S., Geophysical Research Letters, 28, 2077–2080, https://doi.org/10.1029/2000GL012745, 2001.

Folland, C. K., Knight, J., Linderholm, H. W., Fereday, D., Ineson, S., and Hurrell, J. W.: The summer North Atlantic Oscillation: Past, present, and future, Journal of Climate, 22, 1082–1103, https://doi.org/10.1175/2008JCLI2459.1, 2009.

García-Serrano, J., Cassou, C., Douville, H., Giannini, A., and Doblas-Reyes, F. J.: Revisiting the ENSO teleconnection to the Tropical North Atlantic, Journal of Climate, 30, 6945–6957, https://doi.org/10.1175/JCLI-D-16-0641.1, 2017.

Granger, C. W.: Investigating causal relations by econometric models and cross-spectral methods, Econometrica, 37, 424–438, https://doi.org/10.2307/1912791, 1969.

Hagan, D. F. T., Dolman, H. A. J., Wang, G., Lim Kam Sian, K. T. C., Yang, K., Ullag, W., and Shen, R.: Contrasting ecosystem constraints on seasonal terrestrial CO2 and mean surface air temperature causality projections by the end of the 21st century, Environmental Research Letters, 17, 124 019, https://doi.org/10.1088/1748-9326/aca551, 2022.

Hamouda, M. E., Pasquero, C., and Tziperman, E.: Decoupling of the Arctic Oscillation and North Atlantic Oscillation in a warmer climate, Nature Climate Change, 11, 137–142, https://doi.org/10.1038/s41558-020-00966-8, 2021.

Horel, J. D. and Wallace, J. M.: Planetary-scale atmospheric phenomena associated with the Southern Oscillation, Monthly Weather Review, 109, 813–829, https://doi.org/10.1175/1520-0493(1981)109<0813:PSAPAW>2.0.CO;2, 1981.

Huang, Y., Franzke, C. L. E., Yuan, N., and Fu, Z.: Systematic identification of causal relations in high-dimensional chaotic systems: application to stratosphere-troposphere coupling, Climate Dynamics, 55, 2469–2481, https://doi.org/10.1007/s00382-020-05394-0, 2020.

Jiang, S., Hu, H., Lei, L., and Bai, H.: Multi-source forcing effects analysis using Liang–Kleeman information flow method and the community atmosphere model (CAM4.0), Climate Dynamics, 53, 6035–6053, https://doi.org/10.1007/s00382-019-04914-x, 2019.

Kaplan, A., Cane, M., Kushnir, Y., Clement, A., Blumenthal, M., and Rajagopalan, B.: Analyses of global sea surface temperature 1856-1991, Journal of Geophysical Research, 103, 18 567–18 589, https://doi.org/10.1029/97JC01736, 1998.

Krakovská, A. and Hanzely, F.: Testing for causality in reconstructed state spaces by an optimized mixed prediction method, Physical Review E, 94, 052 203, https://doi.org/10.1103/PhysRevE.94.052203, 2016.

Krakovská, A., Jakubík, J., Chvosteková, M., Coufal, D., Jajcay, N., and Paluš, M.: Comparison of six methods for the detection of causality in a bivariate time series, Physical Review E, 97, 042 207, https://doi.org/10.1103/PhysRevE.97.042207, 2018.

Kretschmer, M., Coumou, D., Donges, J. F., and Runge, J.: Using causal effect networks to analyze different Arctic drivers of midlatitude winter circulation, Journal of Climate, 29, 4069–4081, https://doi.org/10.1175/JCLI-D-15-0654.1, 2016.

Liang, X. S.: Unraveling the cause-effect relation between time series, Physical Review E, 90, 052 150, https://doi.org/10.1103/PhysRevE.90.052150, 2014.

Liang, X. S.: Normalizing the causality between time series, Physical Review E, 92, 022 126, https://doi.org/10.1103/PhysRevE.92.022126, 2015.

Liang, X. S.: Information flow and causality as rigorous notions ab initio, Physical Review E, 94, 052 201, https://doi.org/10.1103/PhysRevE.94.052201, 2016.

Liang, X. S.: Normalized multivariate time series causality analysis and causal graph reconstruction, Entropy, 23, 679, https://doi.org/10.3390/e23060679, 2021.

Liang, X. S. and Kleeman, R.: Information transfer between dynamical system components, Physical Review Letters, 95, 244 101, https://doi.org/10.1103/PhysRevLett.95.244101, 2005.

Liang, X. S., Xu, F., Rong, Y., Zhang, R., Tang, X., and Zhang, F.: El Niño Modoki can be mostly predicted more than 10 years ahead of time, Scientific Reports, 11, https://doi.org/110.1038/s41598-021-97111-y, 2021.

Lorenz, E. N.: Deterministic nonperiodic flow, Journal of the Atmospheric Sciences, 20, 130–141, https://doi.org/10.1175/1520-0469(1963)020<0130:DNF>2.0.CO;2, 1963.

Manshour, P., Balasis, G., Consolini, G., Papadimitriou, C., and Paluš, M.: Causality and information transfer between the solar wind and the magnetosphere–ionosphere system, Entropy, 23, 390, https://doi.org/10.3390/e23040390, 2021.

Mantua, N. J., Hare, S. R., Zhang, Y., Wallace, J. M., and Francis, R. C.: A Pacific interdecadal climate oscillation with impacts on salmon production, Bulletin of the American Meteorological Society, 78, 1069–1080, https://doi.org/10.1175/1520-0477(1997)078<1069:APICOW>2.0.CO;2, 1997.

Mosedale, T. J., Stephenson, D. B., Collins, M., and Mills, T. C.: Granger causality of coupled climate processes: Ocean feedback on the North Atlantic Oscillation, Journal of Climate, 19, 1182–1194, 2006.

Paluš, M. and Vejmelka, M.: Directionality of coupling from bivariate time series: How to avoid false causalities and missed connections, Physical Review E, 75, https://doi.org/10.1063/1.5019944, 2007.

610   Paluš, M., Komárek, V., Hrnčíř, Z., and Štěrbová, K.: Synchronization as adjustment of information rates: Detection from bivariate time series, Physical Review E, 63, https://doi.org/110.1103/PhysRevE.63.046211, 2001.

Paluš, M., Krakovská, A., Jakubík, J., and Chvosteková, M.: Causality, dynamical systems and the arrow of time, Chaos, 28, https://doi.org/10.1063/1.5019944, 2018.

Pfleiderer, P., Schleussner, C.-F., Geiger, T., and Kretschmer, M.: Robust predictors for seasonal Atlantic hurricane activity identified with
615   causal effect networks, Weather and Climate Dynamics, 1, 313–324, https://doi.org/10.5194/wcd-1-313-2020, 2020.

Pires, C., Docquier, D., and Vannitsem, S.: A general theory to estimate information transfer in nonlinear systems, arXiv, https://doi.org/10.48550/arXiv.2307.10623, 2023.

Runge, J.: Causal network reconstruction from time series: From theoretical assumptions to practical estimation, Chaos, 28, https://doi.org/10.1063/1.5025050, 2018.

620   Runge, J., Bathiany, S., Bollt, E., Camps-Valls, G., Coumou, D., Deyle, E., Glymour, C., Kretschmer, M., Mahecha, M. D., Munoz-Mari, J., van Nes, E. H., Peters, J., Quax, R., Reichstein, M., Scheffer, M., Scholkopf, B., Spirtes, P., Sugihara, G., Sun, J., Zhang, K., and Zscheischler, J.: Inferring causation from time series in Earth system sciences, Nature Communications, 10, 2553, https://doi.org/10.1038/s41467-019-10105-3, 2019a.

Runge, J., Nowack, P., Kretschmer, M., Flaxman, S., and Sejdinovic, D.: Detecting and quantifying causal associations in large nonlinear
625   time series datasets, Science Advances, 5, https://doi.org/10.1126/sciadv.aau4996, 2019b.

Schreiber, T.: Measuring information transfer, Physical Review Letters, 85, 461–464, https://doi.org/10.1103/PhysRevLett.85.461, 2000.

Silini, R. and Masoller, C.: Fast and effective pseudo transfer entropy for bivariate data-driven causal influences, Scientific Reports, 11, https://doi.org/10.1038/s41598-021-87818-3, 2021.

Silini, R., Tirabassi, G., Barreiro, M., Ferranti, L., and Masoller, C.: Assessing causal dependencies in climatic indices, Climate Dynamics,
630   https://doi.org/10.1007/s00382-022-06562-0, 2022.

Simon, A., Gastineau, G., Frankignoul, C., Lapin, V., and Ortega, P.: Pacific Decadal Oscillation modulates the Arctic sea-ice loss influence on the midlatitude atmospheric circulation in winter, Weather and Climate Dynamics, 3, 845–861, https://doi.org/10.5194/wcd-3-845-2022, 2022.

Small, R. J., Bryan, F. O., Bishop, S. P., Larson, S., and Tomas, R. A.: What drives upper-ocean temperature variability in coupled climate
635   models and observations, Journal of Climate, 33, 577–596, https://doi.org/10.1175/JCLI-D-19-0295.1, 2020.

Soulard, N., Lin, H., and Yu, B.: The changing relationship between ENSO and its extratropical response patterns, Scientific Reports, 9, https://doi.org/10.1038/s41598-019-42922-3, 2019.

Spirtes, P., Glymour, C., and Scheines, R.: Causation, Prediction, and Search (Second Edition), The MIT press, Boston, https://doi.org/10.7551/mitpress/1754.001.0001, 2001.

640   Subramaniyam, N. P., Donner, R. V., Caron, D., Panuccio, G., and Hyttinen, J.: Causal coupling inference from multivariate time series based on ordinal partition transition networks, Nonlinear Dynamics, 105, 555–578, https://doi.org/10.1007/s11071-021-06610-0, 2021.

Sugihara, G., May, R., Ye, H., Hsieh, C.-H., Deyle, E., Fogarty, M., and Munch, S.: Detecting causality in complex ecosystems, Science, 338, 496–500, https://doi.org/10.1126/science.1227079, 2012.

Timmermann, A. et al.: El Niño–Southern Oscillation complexity, Nature, 559, 535–545, https://doi.org/10.1038/s41586-018-0252-6, 2018.

645 Tirabassi, G., Masoller, C., and Barreiro, M.: A study of the air–sea interaction in the South Atlantic Convergence Zone through Granger causality, International Journal of Climatology, 35, 3440–3453, https://doi.org/10.1002/joc.4218, 2015.

van Nes, E. H., Scheffer, M., Brovkin, V., Lenton, T. M., Ye, H., Deyle, E., and Sugihara, G.: Causal feedbacks in climate change, Nature Climate Change, 5, 445–448, https://doi.org/10.1038/NCLIMATE2568, 2015.

Vannitsem, S. and Ekelmans, P.: Causal dependences between the coupled ocean–atmosphere dynamics over the tropical Pacific, the North 650 Pacific and the North Atlantic, Earth System Dynamics, 9, 1063–1083, https://doi.org/10.5194/esd-9-1063-2018, 2018.

Vannitsem, S. and Liang, X. S.: Dynamical dependencies at monthly and interannual time scales in the climate system: Study of the North Pacific and Atlantic regions, Tellus A, 74, 141–158, https://doi.org/10.16993/tellusa.44, 2022.

Vannitsem, S., Dalaiden, Q., and Goosse, H.: Testing for dynamical dependence: Application to the surface mass balance over Antarctica, Geophysical Research Letters, 46, 12 125–12 135, https://doi.org/10.1029/2019GL084329, 2019.

655 Zhang, Y., Wallace, J. M., and Battisti, D. S.: ENSO-like interdecadal variability: 1900–93, Journal of Climate, 10, 1004–1020, https://doi.org/10.1175/1520-0442(1997)010<1004:ELIV>2.0.CO;2, 1997.
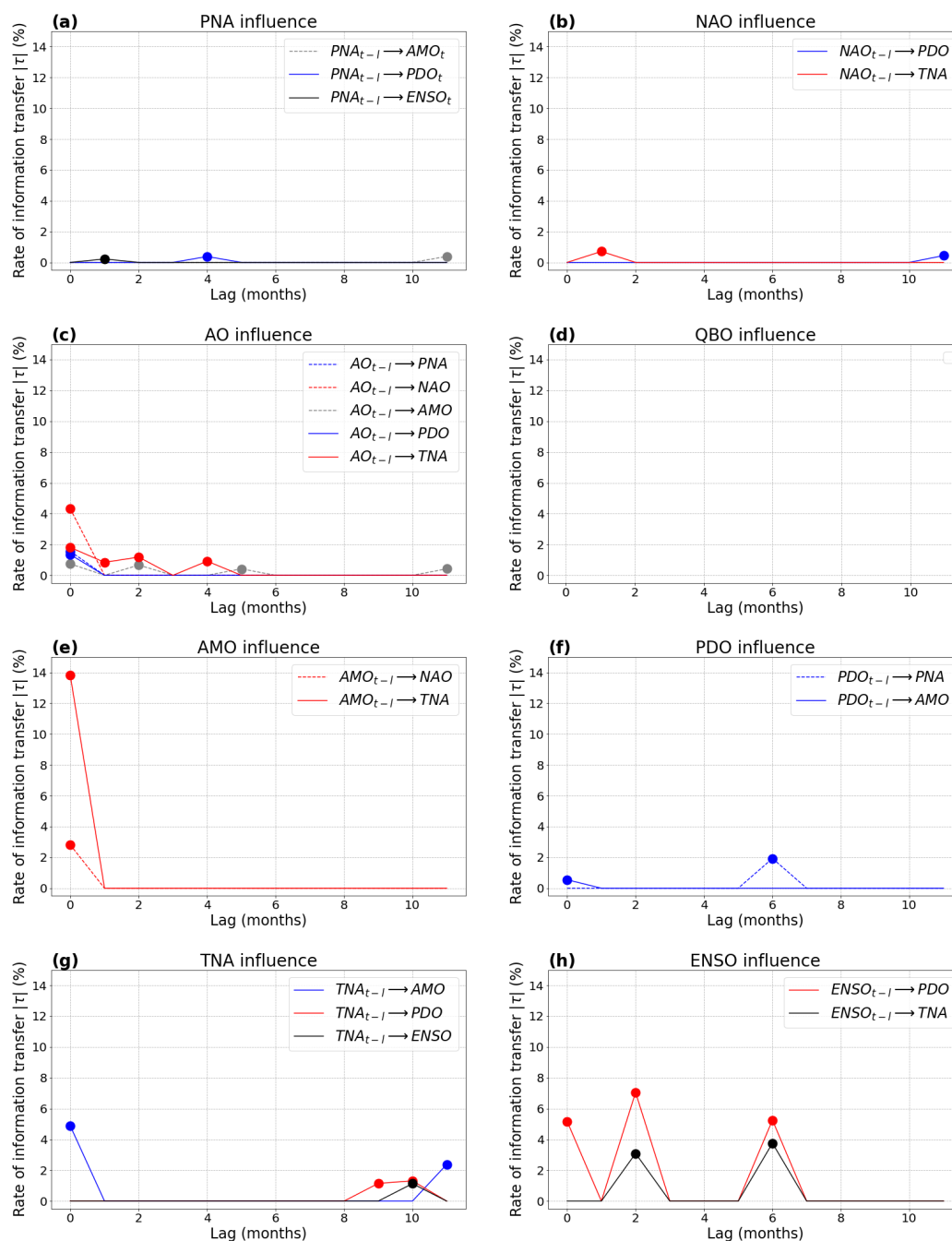
Figure 9. Results from the real-case study with LKIF (rate of information transfer; absolute value) as a function of the lag: (a) PNA influence on the other variables; (b) NAO influence; (c) AO influence; (d) QBO influence; (e) AMO influence; (f) PDO influence; (g) TNA influence; (h) ENSO influence. Only significant influences at the $\alpha = 5\%$ level are shown as filled dots.
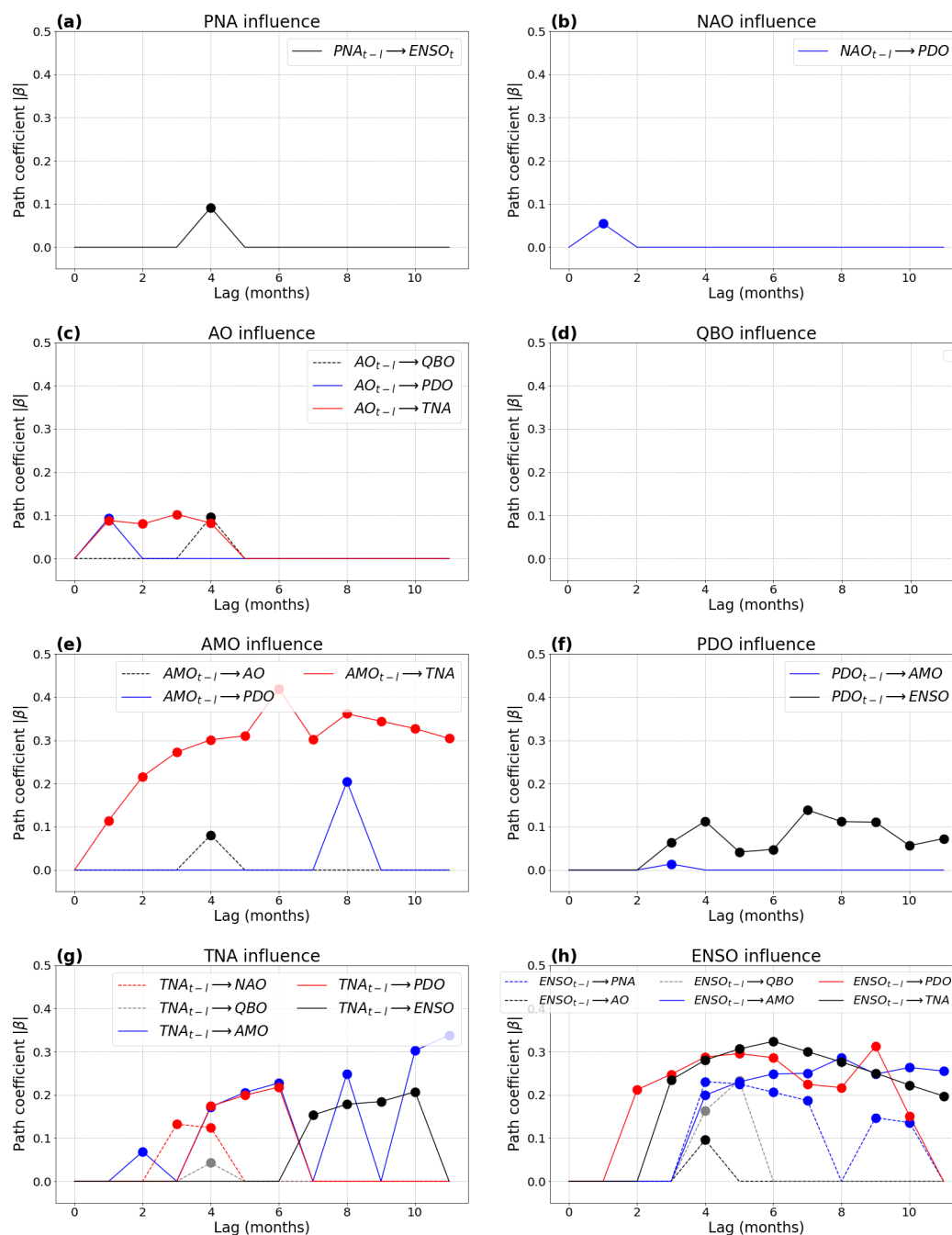
Figure 10. Results from the real-case study with PCMCI (path coefficient; absolute value) as a function of the lag: (a) PNA influence on the other variables; (b) NAO influence; (c) AO influence; (d) QBO influence; (e) AMO influence; (f) PDO influence; (g) TNA influence; (h) ENSO influence. Only significant influences at the $\alpha = 5\%$ level are shown as filled dots.